AD-A133 081 DECOUPLING ION EFFICIENCY FROM IMPEDANCE IN PULSED 1/1
POWER DIODES(U) NAVAL RESEARCH LAB WASHINGTON DC
R J BARKER ET AL. 14 SEP 83 NRL-MR-5184
UNCLASSIFIED F/G 9/1 NL

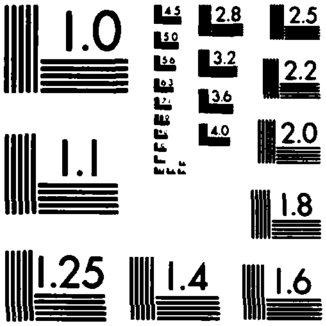

MICROCOPY RESOLUTION TEST CHART
NATIONAL BUREAU OF STANDARDS-1963-A

(2)

NRL Memorandum Report 5184

Decoupling Ion Efficiency from Impedance in Pulsed Power Diodes

R. J. BARKER* AND SHYKE A. GOLDSTEIN†

*Mission Research Corp.
Alexandria, VA 22312

†JAYCOR, Inc.
Alexandria, VA 22304

AD-A133 082

September 14, 1983

This work was sponsored by the Defense Nuclear Agency under Subtask T99QAXLA, work unit 00038, and work unit title "Advanced Simulation Concepts," and by the U.S. Department of Energy.

NAVAL RESEARCH LABORATORY
Washington, D.C.

SECURITY CLASSIFICATION OF THIS PAGE (When Data Entered)

REPORT DOCUMENTATION PAGE		READ INSTRUCTIONS BEFORE COMPLETING FORM
1. REPORT NUMBER NRL Memorandum Report 5184	2. GOVT ACCESSION NO.	3. RECIPIENT'S CATALOG NUMBER
4. TITLE (and Subtitle) DECOUPLING ION EFFICIENCY FROM IMPEDANCE IN PULSED POWER DIODES		5. TYPE OF REPORT & PERIOD COVERED Interim report on a continuing problem.
		6. PERFORMING ORG. REPORT NUMBER
7. AUTHOR(s) R. J. Barker* and Shyke A. Goldstein†		8. CONTRACT OR GRANT NUMBER(s)
9. PERFORMING ORGANIZATION NAME AND ADDRESS Naval Research Laboratory Washington, DC 20375		10. PROGRAM ELEMENT, PROJECT, TASK AREA & WORK UNIT NUMBERS DE-A108-79DP40092, Mod A015, Task 20, 89X0220, 47-0879-03
11. CONTROLLING OFFICE NAME AND ADDRESS		12. REPORT DATE September 14, 1983
		13. NUMBER OF PAGES 59
14. MONITORING AGENCY NAME & ADDRESS(if different from Controlling Office)		15. SECURITY CLASS. (of this report) UNCLASSIFIED
		15a. DECLASSIFICATION/DOWNGRADING SCHEDULE

16. DISTRIBUTION STATEMENT (of this Report)

Approved for public release; distribution unlimited.

17. DISTRIBUTION STATEMENT (of the abstract entered in Block 20, if different from Report)

18. SUPPLEMENTARY NOTES

*Present address: Mission Research Corp., Alexandria, VA 22312
†Present address: JAYCOR, Inc., Alexandria, VA 22304

(Continues)

19. KEY WORDS (Continue on reverse side if necessary and identify by block number)

Diode impedance
Ion efficiency
Numerical simulation
Pulsed power

20. ABSTRACT (Continue on reverse side if necessary and identify by block number)

Classical axial diode theory links the impedance of a diode to its ion production efficiency (i.e., the fraction of diode power carried by ions). This linkage stems from the dependence of both impedance and efficiency on the "aspect ratio" of the given device. This ratio is defined as the cathode outer radius, R, divided by the axial anode-cathode (A-K) gap, D. Numerical simulations and experiments have been completed which demonstrate that the ion efficiency, η_i, is strictly proportional only to the typical pathlength, L, of electrons

(Continues)

DD FORM 1 JAN 73 1473 EDITION OF 1 NOV 65 IS OBSOLETE
S/N 0102-014-6601

SECURITY CLASSIFICATION OF THIS PAGE (When Data Entered)

eta sub i)

18. Supplementary Notes (Continued)

This work was sponsored by the Defense Nuclear Agency under Subtask T99QAXLA, work unit 00038, and work unit title "Advanced Simulation Concepts," and by the U.S. Department of Energy.

20. Abstract (Continued)

eta sub i sub d [illegible]

sub d

in the A-K gap and that this length need not be related to R. Specifically, a radial pinch-reflex diode geometry is examined in which the anode is a cylindrical shell of radius, R + D and of length 2L. For this device, η_i is found to vary as L/D while the impedance, Z_d, varies as R/D. This decoupling of η_i from Z_{diode} offers significant new possibilities for high power/high voltage intense ion beam sources as well as for high power/low voltage intense electron beam sources. A series of numerical simulations using the PREMAS diode-modeling code have been completed for diode geometries which demonstrate both of these applications. Preliminary experimental results confirm the theory as well as the numerical predictions.

CONTENTS

DECOUPLING ION EFFICIENCY FROM IMPEDANCE IN PULSED POWER DIODES

I. INTRODUCTION

Nearly a decade has elapsed since the Intense Ion Beam Research Group at NRL first clearly outlined the important role light ions play in the physics of pulsed-power diode operation.[1] Building upon a theoretical understanding of the nature of electron flow in the diodes[2] coupled with a storehouse of experimental observations[3,4] the group developed a semi-empirical prediction of net diode current in the form of[5]

$$I = I_e + I_i \approx 9(\gamma^2 - 1)^{1/2} \frac{R}{D} \left[1 + \left(\frac{eV}{2m_i c^2}\right)^{1/2} \frac{R}{D} \right] \quad (1)$$

where $\gamma = 1 + \frac{V(\text{in MV})}{0.511}$, R = cathode radius, D = axial anode-cathode (A-K) gap, V = diode voltage, and m_i = ion mass. Implicit in this formula is an ion-to-electron current ratio which may be approximated by[6]

$$\frac{I_i}{I_e} > 0.5 \frac{v_i}{c} \frac{R}{D} \quad (2)$$

where v_i is the maximum ion velocity and the electrons are assumed to have been instantaneously accelerated to near-light velocities. According to these two expressions and for a fixed machine voltage, the diode impedance, V/I, will vary inversely with the aspect ratio, R/D, while the relative proportions of diode current carried by the ions will vary directly with R/D.

In order to understand the physics of Eqs. (1) and (2) it is useful to refer to a schematic picture of a representative axial geometry pulsed-power diode. (The distinction between axial and radial geometries is given by the orientation of their respective primary anode-cathode gap. The radial geometry will be discussed later.) Figure 1 depicts the nature of electron

Manuscript approved July 22, 1983.

and ion flow in the diode. First consider the case of electrons flowing in the absence of ions, $I_i = 0$. It has been shown[7] that the largest fraction of electron current is emitted from the "edge" portions (i.e., $r \approx R$) of the cathode. The emitting surfaces at those large radii benefit from two-dimensional enhancement of the normal electric field while the regions at lower radii experience field strength reductions due to the large amounts of electron space charge emitted at larger radii. Thus, the combination of enhanced electron emission current density with the larger emission area makes the behavior of the electron flow at $r \approx R$ crucial to the final operating state of the diode as a whole. The azimuthal magnetic field generated by the diode current flowing within that radius plays a role equal to that of the electric field in determining the trajectories of those outer electrons. It is this feedback loop between the diode current, electron emission at $r \approx R$, and $B_\theta(r \approx R)$ that provides the rational for Eq. (1). To be specific, if the net current exceeds some "critical" value, I_{crit}, then B_θ in the outer radial regions will cause the mean Larmor radius of electrons there to be less than the anode-cathode gap spacing, D. In that case, those outer electrons will not be able to cross directly from the cathode to the anode but rather will be turned around toward the cathode again at some lower radius where their additional negative space charge will cause reduced electron emission. The reduced electron current, I_e, will lower $B_\theta(r \approx R)$ thus enlarging the mean Larmor radius until it again exceeds the gap, D, and allows direct electron streaming to the anode. Further weakening of B_θ beyond that value is resisted by the again unimpeded electron emission at lower radii. This reasoning argues in favor of an equilibrium I_e value in the neighborhood of an I_{crit} for which the resultant mean electron Larmor radius at $r \approx R$ just equals the gap size, D. After some algebra this "critical current" in kA may be written as[8]

$$I_{crit} = 8.5\ \beta_e \gamma_e \frac{R}{D} \qquad (3)$$

where β_e and γ_e are the standard relativistic quantities for electrons in the diode at voltage, V. Although recent theoretical and experimental work[9] indicates that attention to electrode shaping and to ion space charge distribution can boost electron currents almost a factor of two above I_{crit}, it still serves as a scaling guideline for diode operating parameters. Thus the premise for Eq. (1) remains intact aside from a possible change in the proportionality factor.

The rationale underlying Eq. (2) can likewise be explained by reference to Fig. 1. Stated simply, the relative emission of ions and electrons from their respective electrodes is a function of the electric field strengths normal to the electrode surfaces in the A-K (anode-cathode) gap. Those fields, in turn, depend not only upon the diode voltage, V, and A-K gap spacing, D, but also upon the relative amounts of ion and electron space charge in the gap. Therefore, the ion-to-electron current ratio will depend inversely on the relative "dwell times" of the respective species in the active A-K gap region. The dwell time ratio may be expressed as τ_e/τ_i. In the pinched-beam mode, the predominant flow of electrons from the outer cathode radii will travel about a distance, R, through the A-K gap at about a uniform velocity, c, for diode voltages of a megavolt or more. The emitted ions, on the other hand, are hardly perturbed at all from simple paraxial, straight-line flow through the gap across its width, D. For a diode potential difference, V, they will attain velocities of $[2\ eV/m_i]^{1/2}$. This reasoning leads to a restatement of Eq. (2) in the form

$$\frac{I_i}{I_e} \alpha \frac{\tau_e}{\tau_i} \approx \left[\frac{eV}{2m_i c^2}\right]^{1/2} \frac{R}{D} \quad . \tag{4}$$

The situation changes significantly when, instead of considering the axial diode configuration of Fig. 1, one turns to a radial diode configuration such as that in Fig. 2. In this new orientation, the total diode current can be assumed to ideally split evenly on either side of the diode centerplane. (The stability of such an even current division remains to be rigorously tested.) These currents will generate an azimuthal magnetic field, B_θ, in the A-K gap analogous to that present in the axial diode. Thus, it can be expected that the current on either side of the half-plane will face the same I_{crit} limitation as that expressed in Eq. (3) for the total axial diode current. Therefore, in the case of the radial diode, $I_{diode} \approx I_{crit}$ and the diode impedance is still inversely linked to the ratio of R/D.

This correspondence between the two diode geometries breaks down when one now attempts to approximate the ion-to-electron current ratio. It can again be assumed that I_i/I_e will be inversely proportional to the respective species "dwell times". Here again the ion dwell time, τ_i, can be approximated by $[eV/(2m_i)]^{1/2}/D$. The electron flow, on the other hand, is no longer collapsing radially inward under the action of B_θ and E_z. Rather, the electric field is now dominated by E_r so that the electrons are now being forced to drift to the centerplane. They must therefore cover a distance, L, instead of R and they now enjoy dwell times more closely approximated by $\tau_e \approx L/c$. Thus, the ion generation efficiency of the diode no longer depends upon R/D and, thereby, is no longer directly linked to the diode impedance. The implications of such a decoupling are highly significant to researchers seeking to maximize either ion beam or electron beam production for a diode with fixed impedance parameters.

This report will present numerical simulations of example diode geometries for both the enhanced ion current as well as for the enhanced electron current cases. The numerical findings will be compared to theoretical predictions as well as to the experimental observations currently available. The geometry for the enhanced ion current case was based on a design proposed for the joint NRL-Sandia SHEPERD (Self-magnetically Healing Equatorial Pinch Electron-reflexing Radial Diode) project.[10] The simulations confirmed assumptions regarding the nature of ion and electron flow in the A-K gap. Furthermore, experiments conducted on the Gamble II pulsed power generator to test the geometry confirmed the strong dependence of the impedance, Z, on L. The second set of simulations focused on the problem of minimizing ion production and maximizing the electron current in a low impedance diode. Here, the simulations demonstrated unequivocally that I_i/I_e was tracking L/D and not R/D. For this enhanced electron case, a subset of simulations was conducted to demonstrate that the physics of the L/D dependence could be translated to a diode in axial geometry as well by properly routing the diode return current flow path with respect to the A-K gap. Implications of the overall results for several applications are then discussed.

II. ENHANCED ION CURRENT

Much research in the field of light ion inertial confinement fusion has been devoted to the problem of boosting ion efficiency in high impedance diodes.[11,12] A switch from axial to radial geometry holds promise for being the final solution.

To test the physical assumptions regarding the nature of electron flow in the radial, pinched-beam model, the geometry depicted in Fig. 3 was chosen as a subject for numerical simulation. The cathode radius, R, was taken as 5.0 cm to equal the gap half-width, L, of 5.0 cm. The radial A-K gap itself was fixed at 0.2 cm while the side-gap in the magnetically insulated triplate power feed was set at 0.9 cm. Two types of anode surfaces were studied. The first was a completely solid, electron-absorbing surface spaced 0.2 cm away from the cathode and along which the axial extent of the ion emission could be varied. (Note that complete mirror symmetry about the diode center plane was assumed at all times.) The simulation of the diode was then repeated assuming this time that the front anode surface was a thin (~ 5 mil polyethylene) foil held at full anode potential and through which 1.5 MeV electrons could easily travel. This foil becomes a plasma sheet when the diode is in operation. Behind the foil was a full 0.4 cm radial gap separating it from the solid anode surface. This is the configuration shown in Fig. 3. There was assumed to be zero electric field in the gap behind the foil but the full B_θ due to any axial currents below that radius could be felt there. Thus, electrons penetrating through the foil from the A-K gap could be expected to experience a bending force due to the B_θ behind the foil. If that magnetic field is strong enough, the electrons could be completely turned around and reinjected through the foil back into the radial A-K gap. This is completely analogous to the electron behavior in the axial pinch-reflex diodes pioneered by NRL.[13] Such electron reflexing, if shown to occur for this geometry, can be expected to further enhance the production of light ion flux from the diode.

To examine the behavior of this new diode configuration for the cases described above, numerical simulations were conducted using NRL's PREMAS computer code. As the successor to DIODE2D, the new PREMAS code embodies all of its predecessor's accuracy and efficiency in characterizing steady state, self-consistent ion and electron flows in pulsed power diodes. In addition to those attributes, it also has an unparalleled flexibility in dealing with a huge array of axial and radial diode geometries. Finally, it boasts a completely new diagnostics package based on the powerful DISSPLA graphics software system. The details of the code's field-solving and particle-pushing algorithms may be found elsewhere.[14]

It is sufficient here to point out that PREMAS calculates equilibrium electric and magnetic field strengths over an NZ x NR mesh of discrete data points on a predetermined computational region lying on a arbitrary R - Z planar cross section passing through the diode's centerline. (Note, however, that the lower boundary of the computational region itself need not correspond to the centerline. Rather, it is free to lie at some nonzero value of the physical diode radius.) Complete azimuthal symmetry is assumed. A finite number of macroelectrons and macroprotons having correct, physical charge-to-mass ratios are advanced timestep-by-timestep across the mesh in a relativistically covariant manner. A self-consistent, steady-state solution is sought both for field structures as well as for particle flows. The time-dependent Maxwell's Equations are not observed.

For this specific problem, the physical volume simulated by the PREMAS code corresponded to the "left half" of the A-K gap region of the Fig. 3 diode. This numerical model region is depicted in Fig. 4. Numerical cell spacings of $\Delta R x \Delta Z$ = 0.01 x 0.023 cm were chosen to fill the computational region. Thus the number of axial and radial grid points are 256 and 60, respectively, to fill the 5.9 by 0.6 cm physical space. Allowing a monolayer of "quard cells" surrounding the entire perimeter of the region gives a total cell count of NZ2 x NR2 = 258 x 62 = 15,996 cells. In all cases, the lower boundary was the cylindrical, solid cathode surface at R = 5.0 cm which was held fixed at zero voltage. Similarly, the "left" boundary was always the planar, solid cathode surface designated to be z = 0.0 and also held to zero voltage. For the solid anode case, the upper boundary was at R = 5.2 cm while for the case with the reflexing foil it was set back to R = 5.6 cm. For both cases the electrostatic boundary potential there was graded linearly for Z = 0.0 to Z = 0.9 cm from $\phi = 0$ to $\phi = + 1.5$ MV. The rest of the upper boundary was maintained at full anode potential at $\phi = +1.5$ MV. The treatment of the "right" boundary lying on the diode centerplane is a bit more complicated. As already stated, the right half of the diode is assumed to be a mirror image of the left half across the centerplane. Thus, from a computational standpoint this "right" boundary is perfectly reflecting to particle flows. The presence of space charge and current there also prohibits potential values from being fixed along it. The value of ϕ will change there during the simulation so it is allowed to "float" from timestep to timestep in a slightly damped fashion. This "floating ϕ" boundary feature is enforced only in the A-K gap itself (i.e., between R=5.0 and R=5.2) for both cases. For the anode foil case, of course, the "right" boundary between R=5.2 and R=5.6 runs inside the anode conductor and is therefore maintained at a constant $\phi = +1.5$ MV.

The first case involved an analysis of diode operation with a solid, electron-absorbing anode surface in place of the foil. Ion emission along that surface was turned on in successive stages to examine the steady state electron flow for each stage. Initially, only electron emission was permitted. The equilibrium flow is depicted in Fig. 5a. (Note, again, that only half of the diode is treated numerically and that mirror symmetry about the centerplane is assumed.) In this figure, as well as in the others that follow, the radial dimension scale has been exaggerated to show maximum detail in the flow pattern. Two significant results are observed. First, the net electron current in this half-diode is 0.85 MA which is almost identical to the critical current of 0.81 MA. In addition, there is a slight axial deflection of the electron sheath as it crosses the A-K gap. The net inward deflection measured 0.21 cm - almost identical to the gap width of 0.20 cm. This amounts to a near-perfect quarter-cycle of electron gyromotion.

The next question to be considered concerned the possible effects of limited ion emission along the anode surface.[15] Suppose the electron beam, through one physical mechanism or another, creates a plasma along the anode surface it is striking. To simulate that effect, proton emission was "turned on" along a 0.34 cm wide strip from $Z=1.26$ to $Z=1.60$ cm on the solid anode surface immediately surrounding the electron impact zone. The net result is shown in Fig. 5b. Thanks to even the low ion current of 75 kA, enough positive space charge has been introduced into the A-K gap near the electron emission strip to boost I_e to 1.075 MA. This brings the total half-diode current to over $1.4 \times I_{crit}$. As would be expected from this increased diode current, the axial pinching of the electron sheath is more pronounced. The net displacement is now 1.42 cm toward the centerplane. In the next step, the width of the ion emission strip was nearly tripled so that it extended from $Z=1.26$ to $Z=2.30$ cm. The change, as indicated in Fig. 5c was minor. The net ion current did not quite double, but rather rose to 140 kA. Furthermore, in response to the increased strength of B_θ along the outer cathode surface, the net electron current actually dropped to 1.03 MA. Still, the total half-diode current remained at over $1.4 \times I_{crit}$. It was clear from this new steady-state finding that the electron beam would not simply march axially inwards in-step with an expanding zone of ion emission. Some minimum threshold for beam pinching must first be surpassed. This threshold is clearly more than $1.4 \times I_{crit}$.

In order to pass the pinching threshold, ion emission was turned on along the entire solid anode surface from Z=1.26 inward to the diode centerplane. The change was dramatic. As shown in Fig. 5d, the electron sheath displayed classic ExB cycloids while converging to the diode centerplane. In accordance with pinched beam diode theory, the excess negative space charge partially suppressed electron emission while enhancing ion emission to the levels, I_e = 0.75 MA and I_i = 0.50 MA. This gives an ion-to-electron current ratio of 0.67 compared to a theoretical prediction of 0.7 arrived at via Eq. (4). The overall agreement is excellent. This encouraged one further step of investigation. It was found to be true with low impedance axial diodes that the substitution of an electron-transparent anode foil in place of the solid anode would significantly boost the diode's ion production efficiency. That same substitution was tested here and, indeed, complementary results were observed.[16] As illustrated in Fig. 6, a dense sheath of reflexing electrons formed along most of the anode foil surface. This additional negative space-charge enhanced ion emission in the half-diode to 0.7 MA while further reducing the electron current to 0.6 MA. The new ratio, I_i/I_e, of 1.17 was now, as expected, far in excess of the solid anode prediction. As anticipated, the correlation of detailed diode physics between the radial and axial geometries was very strong. Further proof of this can be found in the sample electron trajectory plots of Fig. 7. In order to generate these plots, the electric and magnetic field structures self-consistent with the steady-state particle flows of the diode were "frozen" over the computational mesh. Into this field structure, electron streams were injected at sample electron emission points. The plots show the resultant stream trajectories for five sample cathode emission points. Their behavior compared closely to that of their counterparts in axial geometry.[17] These simulations had therefore shown that there were no unexpected differences between actual electron flow in the radial diode configuration and that postulated in the decoupling theory. The overall numerical results for this radial diode are summarized in Table 1. Encouraged by these results, the next step taken was the initiation of an experimental test of the decoupling mechanism on the Gamble II pulsed power generator.

Table 1: SHEPERD Diode Results

Anode Type	Ion emission	I_e(MA)	I_i(MA)	η_i	Z(Ω)(full Diode)
Solid	None	0.85	0	0	0.88
Solid	Partial	1.075	0.075	0.07	0.65
Solid	Partial	1.03	0.14	0.12	0.64
Solid	Full	0.75	0.50	0.40	0.60
Foil	Full	0.61	0.70	0.53	0.57

The details of the experimental setup may be found elsewhere.[18] Only the immediately relevant points will be related here. To begin with, the nature of the Gamble II machine argued against a test of the full radial diode geometry. To ensure symmetric power flow into both halves of such a diode, a tri-plate vacuum, power transmission line[19] should be employed. This can best be accomplished at Sandia National Laboratories on their PBFA-I device. Gamble II, on the other hand, embodies a conventional, coaxial power feed to its diode load. Barring the use of complicated power feed convolutes, and wishing to capitalize on the power characteristics of the Gamble II machine, it was decided to construct and test a diode which physically represented only half of the full radial pinch-reflex configuration. The diode geometry was split at its centerplane in exact analogy, by coincidence, to the numerical simulation model but, of course, with a perfectly absorbing "centerplane", "right" boundary instead of a perfectly reflecting one. This experimental configuration is depicted in Fig. 8. The power feed is from the left. The anode and cathode structures are clearly shown to approximate scale. In this geometry, the diode radius remained limited to between 6.4 and 7.0 cm while the A-K gap and the all-important half-width, L, could be varied between 0 to 1.0 cm and 5, 10 and 15 cm respectively. Two sets of preliminary findings were derived. First, with the A-K gap, D, fixed at 4.75 mm, electrode structures of three different lengths, L = 5, 10, 15 cm were tested. As shown in Fig. 9a, the impedance was found to be quite insensitive to the ion-efficiency-determining parameter, L. On the other hand, when a fixed L of 10 cm was tested with gap widths, D, of 3.7, 4.8, and 5.9 mm, the impedance still scaled linearly with D as expected from the theory (see Fig. 9b). Thus, for a predetermined, machine dependent impedance, only the radius and A-K gap of a diode need remain fixed while the experimenter is free to vary L to achieve a full range of I_i/I_e ratios as desired. For this particular configuration, optimization of light ion production was the primary consideration. Thus, anode half-widths of up to three times the diode radius were of interest to boost the ion current fraction to about three times that normally realizable in an axial diode of the same impedance. For other applications, the converse problem of minimizing ion production is the major objective. The alternate solution is described in the following section.

III. ENHANCED ELECTRON CURRENT

A. Radial Geometry

To achieve a minimization of relative ion current in a diode of a certain impedance, the same radial diode concept as that shown in Fig. 2 and discussed for the case of ion enhancement in Section II can be employed. First, the diode current and, hence, its impedance is fixed to some desired value by adjusting the R/D ratio found in Eq. (1). Then the ratio of I_i to I_e is minimized by shrinking the half-width, L, using Eq. (4) with L substituted for R. For a certain set of experimental parameters that were of interest for a specific appliction,[20] the diode geometry depicted in Fig. 10 was chosen for study. Note the similarity to the ion diode of Fig. 3. Since a focused flow of electrons is now the prime product of interest, the positions of the cathode and anode have been exchanged. To attain a low impedance (i.e., a high current flux), a cathode radius of 10.0 cm was used in conjunction with a relatively small A-K gap of 0.2 cm. This sets R/D to a value of 50. At the same time, L is kept small, 0.6 cm, leaving an L/D of only 3. Simulations using the PREMAS code were again initiated, as for the previous diode, seeking equilibrium field structures and particle flow characteristics. For this diode, however, the voltage was fixed at 1.0 MV.

To check the details of diode performance, two separate situations were modeled. In the first, only electrons were permitted in the system. In the second, both electron and ion emission were allowed. The numerical computational region used for both situations was very similar to that used for the ion diode of Section II. This new region is depicted in Fig. 11. It extended radially from the solid, cylindrical anode surface at R = 10.0 cm out to R = 10.5 cm, and axially from the left, solid, planar anode surface designated as Z = 0.0 over to the diode centerplane at Z = 0.9 cm. As shown in the figure, it was spanned radially by 50 cells, each 0.01 cm wide, and axially by 64 cells which were 0.0125 cm wide. This gave a total cell count of a modest (64+2) x (50+2) = 3432 cells. Electron emission was permitted from all three surfaces of the protruding, 0.2 cm wide, 0.3 cm long cathode ring as well as from the solid cathode surface radially recessed 0.3 cm from the face of the ring. In the second simulation, the emission of protons was "turned on" over the full 0.9 cm length of the cylindrical anode face.

In running the "electrons-only" case it was again of interest to see how closely the current flow mimicked that normally observed in conventional axial diodes. At the start of the simulation, the equipotential lines in the source-free diode gap were plotted (see Fig. 12a). It is clear from this figure that 2-D enhancement of the normal electric field at the edges of the cathode face is present and that, therefore, enhanced electron emission can be expected there. After electron emission is initiated and steady state operation achieved, the equipotentials readjust themselves to accommodate the accumulations of negative space charge (see Fig. 12b). The Gaussian emission of electrons at the cathode surface forces the normal electric field there to zero, effectively "pushing back" the equipotentials in that vicinity. At the same time, the contours are compressed near the opposing anode surfaces.

To fully characterize the flow of electrons in the A-K gap, four other specific diagnostics were output. First of all, the electron current density hitting the anode cylinder as a function of Z is plotted in Fig. 13a. The scatter of data points shows a clear choppiness to the current flow but also indicates a sharp peak at about Z = 0.35 cm, a rough, high plateau between Z = 0.45 to Z = 0.60 cm and a lower peak near the diode centerplane between Z = 0.85 to Z = 0.90 cm. Integration over the half-diode yields an electron current of 1.51 MA which is significantly but not dramatically higher than the theoretical critical current of 1.18 MA. Further insight into the nature of the electron flow is given by the sample, equilibrium electron orbits shown in Fig. 13b. To generate this plot, the steady-state electric and magnetic fields were "frozen" onto the computational mesh. Then streams of electrons were injected into the system from preselected, sample emission points along the cathode surface. The temporal spacing between electrons in each stream was fixed thereby permitting an inspection not only of electron positions but also of relative velocities. Clear from the picture is the effective "focusing" of the electron flow from the outer cathode surface down to the cylindrical anode between Z = 0.3 and Z = 0.4 cm accounting for the peak in $J_e(Z)$ there. The flow from the cylindrical face of the protruding cathode ring likewise hits the anode between Z = 0.4 and Z = 0.6 cm, explaining the roughly constant current density plateau there. Finally, a strong confluence of the sample electron streams takes place near the cathode centerplane. The smooth, uniform nature of the magnetic bending and focusing that the streams experience appears qualitatively obvious from Fig. 13b. A quantitative assessment of this bending is given by Fig. 13c. The tangent of the angle toward the centerplane made by an average electron momentum vector with the surface normal vector was plotted for each mesh point as a function of the axial dimension, Z. The average tangent values are seen to vary only slightly around 1.0 over almost the entire anode impact surface. This indicates that the average electron at almost every value of Z hit at about 45°. Plotting an overall angular distribution function of all electrons hitting the anode over a prolonged period of time yields Fig. 13d. This shows that very nearly every electron hit within a relatively small "window" about 45°. It may be presumed that the predominant cause for the near-zero average tangent values between Z = 0.8 and Z = 0.9 cm was the crossover of electrons from the mirror half-diode on the other side of the centerplane. Electrons from the other side hitting at -45° canceled the tangent values of those hitting at +45°.

At this point, ions (specifically, protons) were introduced into the simulation. This may occur physically if a hydrogen-rich plasma is created along the anode surface. Numerically, ion emission is achieved quite simply by monitoring the normal component of the electric field along a predetermined portion of the anode surface and by introducing sufficient positive charge carriers along that surface to zero that field component. For the purposes of this simulation, such ion emission was "turned on" from Z=0.1 cm all the way through the centerplane of the diode. The results were dramatic and closely paralleled what takes place in a standard axial pinched beam diode. Consider the situation after equilibrium was reached for this combined electron-ion case.

First of all, compare the new steady-state electrostatic potential contour plot shown in Fig. 14a with its electrons-only counterpart in Fig. 12b. Note that the contours that had hugged the anode suface in the earlier plot are now "pushed back" by the emitted ion space charge. The electric field is zeroed along all emission surfaces resulting in an intensification of the radial field midway in the radial A-K gap. Furthermore, the potentials along the cathode's axial gap face have also been swept further back indicating an intensification of the electron current emission there. In fact, as can be expected due to the injection of massive amounts of positive space charge, the overall diode electron current has increased by over 30%. The net average electron current reached an equilibrium value of 4.19 MA in response to the 0.31 MA of ion current (or 2.1 and 0.16 for the half-diode). An even more dramatic change is observed in the axial profile of electron current density impacting the cylindrical anode face. This plot is shown in Fig. 14b. It bears no resemblance to the corresponding plot for electrons-only flow in Fig. 13a. However, the sharply peaked nature of this profile is precisely what one could expect from classic pinched-beam diode operation.

The electron current density hitting the anode peaks at the center due to the radially pinched flow. The central peak of over 500 kA/cm^2 is more than 50 times more intense than J_e opposite the cathode tip (whose axial position is indicated by two dashed lines at $Z=0.3$ and 0.5 cm). Integrated over the entire anode, the net electron current is 4.19 MA, compared with 3.02 MA for the electrons-only case.

If, as in the electrons-only case, most of the electrons were streaming from the cathode to the anode in simple, straight arcs, then one might now expect a peak in the electron angular impact distribution at some large positive value. Specifically, since most electrons will originate at the cathode ring tip ($z \sim 0.3$ cm) and will impact the anode at about $z = 0.9$ cm, the mean tangent could be predicted to be about $(0.9 - 0.3)/0.2$ or +3. In fact, this is not the case. The actual angular distribution shown in Figure 14c depicts a gentle peak well-centered around $\tan \theta = 0.0$. In search of a reason for such a distribution, one first may examine the axial profile of mean impact tangents plotted in Figure 14d. Below $z = 0.7$ cm, electrons end their cross-gap trajectories at consistently sharp angles. Near the centerplane, above $z = 0.75$ cm, however, the mean tangents are clustered around zero as they were in Figure 13c for the electrons-only case. Given the sharp current density peak around the center, it is only reasonable that the overall mean tangent also be about zero. Then the question becomes, why are the mean tangents at the centerplane all about zero? The simple argument regarding electrons crossing over from the "other side" of the centerplane and cancelling large positive tangents with their negative tangents does not apply here. If that were the case here, then the distribution may indeed have an average of zero but it would be approximately, symmetrically double-peaked, perhaps with one peak around + 3.0 and another near - 3.0. The true answer regarding the peak at zero appears, instead, to be the electron orbit randomization illustrated in Figure 15. In this snapshot of steady-state trajectories, the scrambling effect of E x B drift orbits for this pinched beam situation is manifest. Note the multiple figure-eight paths about the centerplane which numerous electrons execute before ending their maneuvers at the anode surface. Such orbit behavior is also observed for axial pinched-beam diodes. This orbit randomization fully justifies a zero mean for tan θ . In fact, the explanation is so strong that one must ask why the distribution of Figure 14c is not precisely centered at 0.0. The reason for that asymmetry is simply that Figure 14c represents a time integration of electrons impacting over just half of the axial anode surface. If this integration had been extended over infinite time and over the entire anode surface, the angular distribution would be absolutely symmetric around zero.

Table 2: Enhanced Electron Radial Diode Results

Species Present	I_e(MA)	I_i(MA)	η_i	Z(Ω)(Full Diode)
Electrons Only	1.51	0	0	0.33
Ion and Electrons	2.08	0.16	0.07	0.22

The results of these two simulation runs are summarized in Table 2. Note that the currents presented in the table are for the half-diode. Multiply by two to obtain the full diode results. Of primary interest is the boosting of diode electron current from 3 MA ($=1.25\ I_{crit}$) to 4.15 MA ($=1.7\ I_{crit}$) through the introduction of ion emission in the radial A-K gap. This enhancement of electron current is highly desirable for specific applications such as x-ray production through bremsstrahlung. What is not desired is a "loss" of too much diode power to unnecessary ion production. Minimization of ion current motivated this particular choice of diode geometry. The ratio, R/D, was set at 10.0/0.2 = 50 to boost I_{crit} (and thereby, I_e) via Eq. (3). At the same time, the diode gap aspect ratio, L/D, was set to 0.6/0.2 = 3 so that Eq. (4) (with L/D substituted for R/D) yields a species current ratio of $I_i/I_e \approx 0.07$. The simulation found a ratio of 0.078 which amounts to excellent agreement with theory. Thus, the "cost" of boosting I_e from 1.25 to 1.7 times I_{crit} may be considered "cheap" in terms of wasted ion current.

There is a problem, however, with this configuration. The radial geometry results in a radial flow of electron current with a resultant radial flux of the bremsstrahlung x-rays. Thus the object to be exposed to the x-rays (say, a patient for medical applications) must be inserted into the hollow anode volume. This places an obvious upper bound on the physical size of the object to be irradiated. In addition, there are high voltage hazard considerations to be dealt with when placing anything into the diode region. These difficulties could be alleviated if this high fluence diode could be configured in an axial rather than radial geometry. Such a change would allow a predominant x-ray flux away from the diode structure which could be focused or defocused to irradiate a small or an extended target. Clearly, a conventional axial diode design will not achieve this objective. The solution, a magnetically insulated splitter (or MIS) diode, was suggested by researchers at Maxwell Laboratories.[21] The essence of this device relied on a rerouting of the diode return current through the inside of the hollow cathode, thus altering the strength of the diode B_θ felt by the electrons as they transit the A-K gap. The MIS concept and a simulation of the basic device are presented in the following section.

B. Axial Geometry

The geometrical translation of the enhanced electron current radial diode discussed in the previous section to a practical axial diode configuaration was straightforward. The key element which spelled success for the radial diode was the physical positioning of the imaginary $B_\theta = 0$ surface within the A-K gap in such a way that it approximately separated one half of the net diode electron current from the other half. Since the $B_\theta = 0$ line traced on the anode surface represents the focus of the pinched electron flow, its position determines the approximate electron "dwell time" in the A-K gap and thus impacts on the ion-to-electron current ratio in accordance with Eq. (4). To achieve this effect in axial geometry, the radial geometry is schematically "rotated". The radial axis is thus transposed with the axial axis. The physical equivalence of the two orientations is achieved by routing half of the net diode current through a conductor located at a radius inside the inner radius of the hollow cathode. This is accomplished in the MIS concept device previously mentioned. In this new geometry, R/D is once again replaced by L/D in the determination of I_i/I_e. However, L is now defined as simply the halfwidth of the hollow cathode cylinder (i.e., one half of the distance between the cathode's inner and outer radius). Once again, a cathode with small L can be used to restrict I_i/I_e while simultaneously keeping R large with respect to D in order to preserve a high total electron current.

To test this concept for axial diode electron enhancement, the geometry depicted in Fig. 16 was modeled. This cathode was taken as a solid ring with a mean radius of 13.0 cm and with axially protruding inner and outer radial edges. These edges protrude about one-eight inch (~ 0.34 cm) out from the solid ring. This ring cathode is almost completely surrounded by a hollow toroidal anode shell. This shell is radially centered on the ring so that its mean radius is also 13.0 cm. A radial A-K gap of 3.0 cm is maintained on either side of the ring. Since the ring has a radial thickness of 1.6 cm, this implies a radial anode thickness of 7.6 cm. Finally, the effective A-K gap (after plasma gap closure) is set at 0.3 cm. In order to mimick an experimentally interesting device, the constant diode voltage is set to 1.5 MV. In constructing the specific numerical model, only the volume spanning the full radial gaps and frontal, axial gap surrounding the two cathode tips is of interest. Thus, the rear planar boundary of the computational region is aligned with the recessed back surface in the interior of the cathode ring. The opposite axial planar boundary as well as the lower and upper radial boundaries are naturally made to coincide with the inner surfaces of the surrounding anode shell. The R-Z cross section of the computational region thus measures 0.64 by 7.59 cm.

The resulting simulation configuration is shown in Fig. 17. Numerical cell spacings of $\Delta R \times \Delta Z = 0.03 \times 0.02$ cm are chosen to fill the modeling region. This results in 32 equispaced cells axially and 253 radially. Allowing a monolayer of "guard cells" surrounding the entire perimeter of the region gives a total cell count of $34 \times 255 = 8670$. The protruding cathode tips are each represented by conducting "surfaces" seven cells wide radially and 17 cells axially. They are maintained at the cathode potential of zero as is that segment of the left boundary which is sandwiched between them. The remaining two segments of the left boundary separating the anode and cathode have fixed logarithmic gradings of potential between zero and +1.5 MV. When the simulation is underway, electron emission is permitted only from the two seven-cell-wide faces of the protruding cathode tips and from the inner surface of the cathode recess. Two separate electrons-only steady states are simulated. In the first, no return current is allowed to flow inside the cathode radius. In the second, exactly half of the diode current is directed along the lower axial boundary which represents the inner conducting surface of the anode shell. In the final run, the 50-50 division of the diode return current is maintained while proton emission is "turned on" along the circular strip of anode surface opposite the ring cathode face.

The simulation region is initialized at t=0 with no charges present and only a fraction of the peak diode voltage imposed. The electrostatic equipotential contours which result in this configuration are shown at 10% intervals in Fig. 18. Note the exceptionally tight compression of the contours in the vicinity of the two tips with the resultant intensification of normal electric field values there. This is a manifestation of the two-dimensional electric field enhancement typical in such hollow cathode devices. As expected, as soon as electron emission is "turned on" intense streams of electron current are ejected from the two protruding tips. At the same time, the low electric fields in the interior region between the two tips cause more than an order-of-magnitude lower emission from the cathode ring's recessed back face. This relatively slow moving mass of electron space charge in this interior region sweeps back the electrostatic potential contours there resulting in a further decrease of the already low electric field and the consequent reduction of electron emission there to a mere trickle. This field-modification process is clearly visable in the equipotential contour plot shown in Fig. 19a as compared with that of Fig. 18. In this new figure, steady-state electron flow is fully established. One thousand timesteps of $0.5\text{x}10^{-12}$ second each have passed and this translates to over five typical electron A-K gap crossing times. The regions of high concentrations of electron space charge manifest themselves not only in the just-mentioned sweep-out of contours from the cathode ring interior but also in the doublehorned distortion of all of the contours where the two principle electron current streams are localized. Keep in mind that all of the diode return current flows along the outside (upper) radial boundary in this run. Therfore, except for effects associated with the protrusion of the anode surface inside the inner radius of the cathode ring, the behavior of this device should closely resemble that of a standard, axial, hollow cathode diode. It does.

Just as in the previous set of simulations for the radial enhanced I_e diode, so too here detailed diagnostics were performed at the anode plane in order to obtain a comprehensive characterization of the electron beam. The first diagnostic of Fig. 19b shows the radial profile of the electron current density striking the anode. As a convenient reference, the radial positions of the two protruding cathode tips on the opposite side of the diode are indicated on the plot with dotted lines. The lines clarify the degree of radial deflection the beams have undergone in their traverse of the axial A-K gap. In a standard hollow cathode diode with suppressed ion flow, one would expect the hollow electron beam to have been pinched radially inward by a distance about equal to the A-K gap. This is consistent with the critical current model explained in Section I. A typical electron may be pictured to have executed a 90° circular arc in the gap transit. Such deflections appear in Fig. 19b. Both beam components are pinched about 0.3 cm inward toward their common centerline after their 0.3 cm axial traverse. Each peak emitted by its respective cathode tip is sharply pronounced with the inner beam carrying more current than the outer beam. The outer cathode tip emits less electron current since it is immersed in the B_θ field generated by the inner cathode tip and beam. This strong B_θ acts to partially insulate emission on the outer tip.[22] As an estimate for the expected net current, one may use Eq.

(3) with $\beta_e \gtrsim 1$, $\gamma_e = 3.935$, $R = 13.0$ cm, and $D = 0.3$ cm. This yields $I_{crit} = 1.45$ MA. If the two costreaming hollow electron beams were indeed independent, this would predict a net diode current of about $2\ I_{crit} = 2.9$ MA. In fact, as just seen, the outer beam is magnetically coupled to the inner one and experiences a current reduction because of it. This helps to explain the net observed diode electron current of 2.16 MA for this case in steady state.

The other major beam diagnostics are concerned with the local and global angular distribution of the electrons incident on the anode face. First, a radial scan of impact angles as a function of the anode radius, r, yields the plot of Fig. 19c At each 0.03 cm wide data cell, the average is taken of the tangent of their impact angle, θ. As expected from the radial pinching, all of the angles are positive. Furthermore, if all of these data points were equally weighted, one would calculate an overall mean impact tangent of slightly over 2.0. However, all points are not of equal weight since the current density profile is far from flat. There are essentially two well-defined hollow beams. From this plot one may assume that the inner beam is represented by the cluster of data points around $\tan\theta \gtrsim 1.0$ below $r = 12.3$ cm. Thus, typical electrons from that beam are striking the anode at about 45°. Similarly, the trace of points above $\tan\theta \approx 2.0$ and $r = 13.0$ cm are due to the electrons of the outer beam. They experience stronger magnetic bending because they feel the B_θ generated by the inner beam, thus they strike the anode at shallower angles (larger θ's with respect to the surface normal). Weighting these mean tangents by their respective current densities from Fig. 19b yields the global angular distribution plot of Fig. 19d. It is the behavior of the more intense inner beam that dominates the overall physics. The distribution peaks slightly below $\tan\theta = 1.0$ similarly to that observed for the corresponding radial diode case.

At this point in the simulation (t = 1000) exactly half of the net diode current at any given time is rerouted along the inner (r = 9.21 cm) surface of the anode "can". The effect on the dual-beam electron flow is exactly as expected. By t = 2000, a near equilibrium for the diode with the 50-50 return current split had been established. The new configuration for the electrostatic equipotential contour surfaces is shown in Fig. 20a. Even from this plot alone the new relative balance between the inner and outer beams is apparent. The former pinching toward the common centerline at r = 0 has given way to complementary pinching toward the imaginary centercylinder surface midway between them at r = 13.0 cm. This phenomenon is confirmed by the electron current density profile shown in Fig. 20b. Not a single data point falls outside the inner and outer cathode ring radii. The two peak densities from the two respective cathode tips are still distinct and still unequal although not nearly to as great a degree as in the previous case. The lack of perfect equality is traced simply to the inequality of the tip radii. The inner tip is at r = 12.2-12.4 cm while the outer one is at r = 13.6-13.8 cm. The currents, though magnetically decoupled, cannot be equal.

An even more dramatic and pleasing manifestation of this new centered pinching mechanism between the cathode tips appears in Fig. 20c of the radial profile of mean impact tangents along the anode face. The profile is nearly perfectly balanced with opposing impacts on opposite sides of r = 13.0 cm. Electrons from the inner tip impact at negative angles ($\tan\theta \sim -1$) while those from the outer tip strike at positive angles ($\tan\theta \sim +1$). In deriving an overall distribution from this radial angular profile once again the radial density profile must provide the relative weighting. Synthesizing Figs. 20b and 20c would lead one to expect a global distribution function with two distinct peaks; one at tan $\theta = -1$ and one near tan $\theta = +1$. That is indeed what results in Fig. 20d. In this case too, the symmetry about the tan $\theta = 0.0$ is far from perfect. Again, this asymmetry may be attributed to the unequal tip radii. The inner tip normally emits more current than the outer when all of the return current flows along the outer anode radius. Therefore, routing half of the total diode current along the inner radius will not totally cancel the inner electron beam current. Some residual B_θ will still remain to insulate some of the electron emission there. Although the decoupling of the two electron flows was not complete, it was still effective enough to boost the net diode I_e to 3.4 MA. This compares well with the 2 I_{crit} value of 2.9 MA calculated earlier. The remaining effect to test is the influence of ion flow on this configuration. Of particular importance is the value of I_i/I_e which will emerge.

This final simulation of the series was accomplished by allowing the emission of protons along the planar anode surface in a ring of inner and outer radius exactly equal to that of the cathode ring. Thus, ion emission is "turned on" between r = 12.2 and r = 13.8 cm. Eighteen hundred additional timesteps are then allowed to pass before this new steady state is assessed. The assessment begins with an examination of the altered equipotential contours in Fig. 21a. The two streams still seem distinct but some turbulence is apparent. The nature of this stream mixing is clarified by the electron current density profile of Fig. 21b. Only one distinct density peak stands out opposite the lower cathode tip. Under the influence of the neutralizing ion space charge, the dual electron beams have pinched together as expected. Once again, since the two beam currents are not equal, the 50% centerline return current cannot center the pinch between the two cathode tips. The electron current for the new steady-state is about 3.87 MA, a significant increase over the electrons-only case. The net ion current measures about 0.19 MA which translates to a diode ion production efficiency of 0.047. By comparison, taking Eq. (4) and replacing R/D with L/D = 0.8/0.3 = 2.67 yields $I_i/I_e \approx 0.075$ and a predicted ion efficiency of $\eta_i = (I_i/I_e)/(1+I_i/I_e) = 0.07$. The agreement is not bad considering the crudeness of the approximations made.

The next question concerns the nature of the new impact angle distribution for the electrons striking the anode surface. Part of the answer lies in Fig. 21c. The plot of mean impact tangents as a function of radius shows that the electrons impacting near the current density peak at 12.21 cm have an average impact tangent of zero. This is precisely analogous to the previous cases studied. The presence of ion space charge transforms the simple electron arc trajectories of the ion-free equilibrium to complicated $\vec{E} \times \vec{B}$ drift orbits which randomize their final impact angles. The scattered data points above r = 12.4 cm with mean tangents of 1.0 and higher represent only sparse current densities (i.e., relatively few macroelectrons). This is borne out again by the overall angular impact distribution plot shown in Fig. 21d. This net distribution of all electrons in the equilibruim configuration is strongly peaked about $\tan\theta = 0.0$. Ion-induced pinched beam electron flow has been achieved although the pinching is not centered between the two cathode rings. Once again, the previously described imbalance between the net emission of the two separate rings causes a net displacement of the pinch radially inward. This shifting of the pinch indicates a mechanism for adjusting the mean electron impact radius not only by altering the percentage of total diode return current routed along the centerline but also by controlling the radial extent of ion emission over the anode face. Allowing ion emission down to smaller radii - say 10 cm - would quite probably draw the pinched cylindrical beam's current density peak even further inward. This would be an interesting topic for further study but is beyond the scope of this report. The results from these MIS diode simulations are summarized in Table 3.

Table 3: MIS Diode Results

Species Present	MIS Current	I_e	I_i	η_i	$Z(\Omega)$
Electrons Only	NO	2.16	0	0	0.69
Electrons Only	50%	3.40	0	0	0.44
Ions and Electrons	50%	3.87	0.19	0.047	0.37

IV. GENERAL CONCLUSIONS

Standard diode theory links both impedance and ion efficiency to the ratio of cathode radius to A-K gap, R/D. This relationship between the two parameters severely limited researchers in their choice of operating regimes. If one desired a high ion production diode, he was restricted to one ohm or sub-ohm levels of operation. Conversely, a project calling for a minimization of ion current in relationship to the electron current dictated a boosting of diode impedance to a multi-ohm level. These restrictions no longer apply. Table 4 presents a synopsis of the major results of all three sets of simulations related in this report. The ion-to-electron current ratios observed in the runs are clearly tracking the cathode half-width to A-K gap ratio, L/D, and not R/D. (Note that the figures presented in the table are all for half-diodes of each configuration.)

Table 4: Summary of Results

Diode Type	Enhanced Ions	Enhanced Electrons	
Geometry	Radial	Radial	Axial
Voltage (MV)	1.5	1.0	1.5
R, D, & L (cm)	5.0, 0.2, 5.0	10.0, 0.2, 0.6	13.0, 0.3, 0.8
R/D and L/D	25 and 25	50 and 3	43.3 and 2.67
I_i/I_e from R/D	0.707	1.15	1.22
I_i/I_e from L/D	0.707	0.069	0.075
Simulation I_i/I_e	0.67	0.074	0.049
Theor. Current (MA)	1.46	1.34	1.59
Sim. Current (MA)	1.25	2.25	2.04
Theor. Impedance (Ω)	1.027	0.746	0.943
Sim. Impedance (Ω)	1.20	0.44	0.735

It is also clear from the table that the enhanced ion production case is not a rigorous test of this technique since R and L are identical. This suggests an interesting follow-on effort. Prior to the research on the SHEPERD diode, significant time and energy had been invested by the NRL Intense Beam group in a DNA-sponsored project to design an efficient ion diode for the AURORA pulsed power generator at the Harry Diamond Laboratory.[23,24] Working at voltages around 3-5 MV and impedances of up to 40 ohms, ion efficiencies of at best 5% to 20% were realized. A radial diode configuration embodying a large L/D but small R/D would hold great promise for achieving 50%+ ion efficiencies at 20 ohm levels. Unfortunately, such a device would be strongly elongated in the axial dimension, causing significant problems in the design of useful "targets." Still, an intense flux of relatively high voltage ions may be of interest for specific applications. In addition, although an axial geometry counterpart is impossible (since L would be restricted to be less than R) some intermediate geometry such as conical or hemispherical may be workable.

ACKNOWLEDGEMENTS

The authors wish to thank Gerald Cooperstein, Steve Stephanakis, Frederick Sandel, Robert Meger, and Paul Ottinger of the NRL-JAYCOR intense beam team as well as Pace VanDevender, Jeffrey Quintenz, Cliff Mendel, and Steven Rosenthal of Sandia National Laboratories in addition to John Shannon, Jay Pearlman, and Nino Periera of Maxwell Laboratories and Major Michael Fellows of the Defense Nuclear Agency for useful discussions during the course of these simulations. This research was performed at the Naval Research Laboratory with the support of the Defense Nuclear Agency and the U.S. Department of Energy.

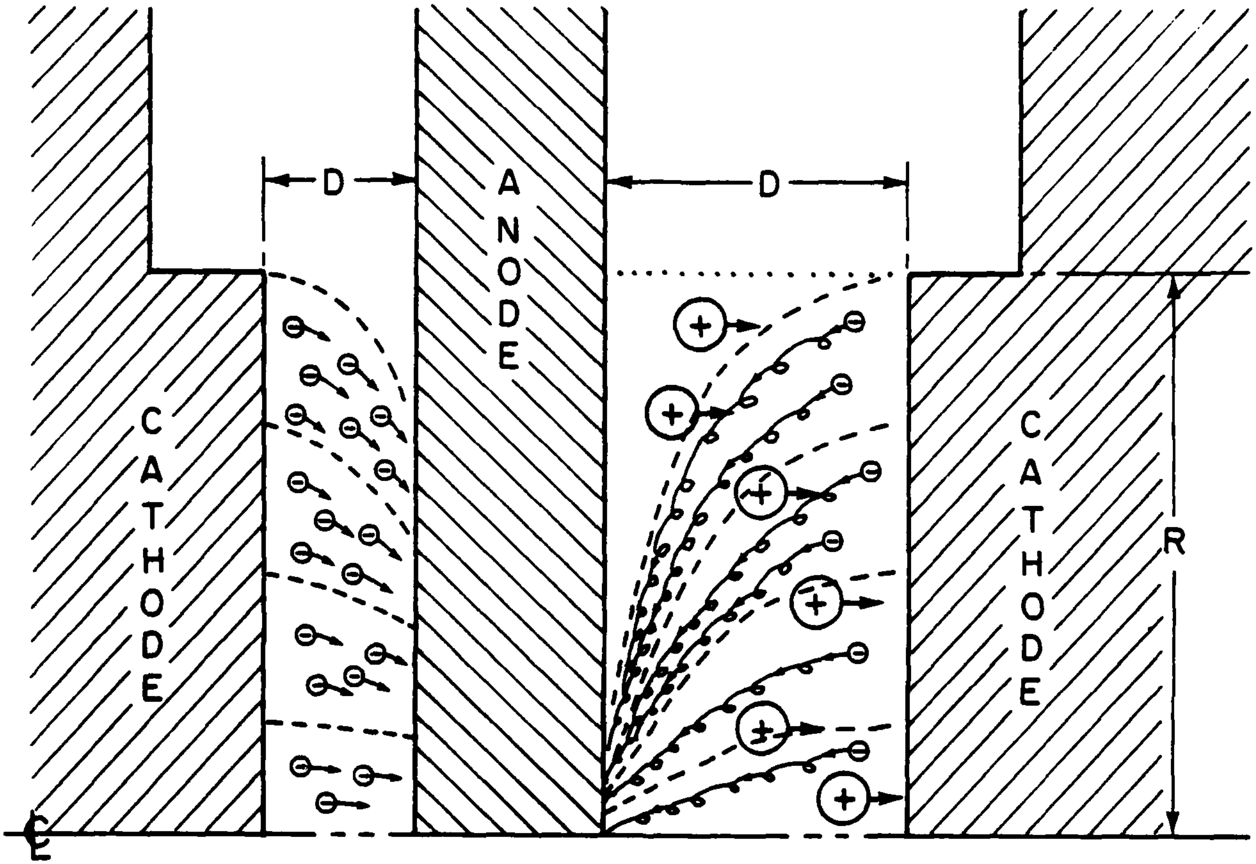

Fig. 1 — Axial diode schematic

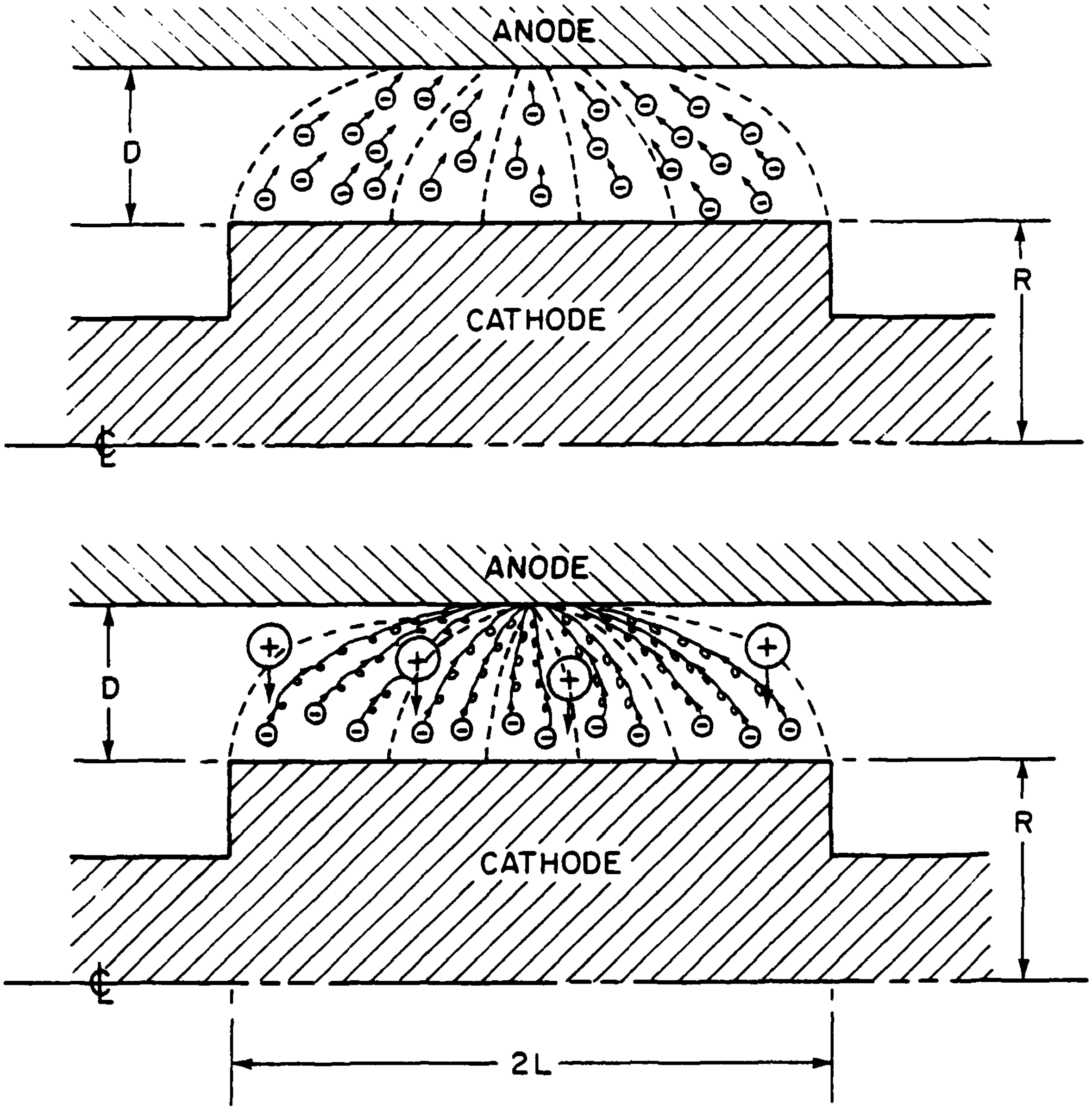

Fig. 2 — Radial diode schematic

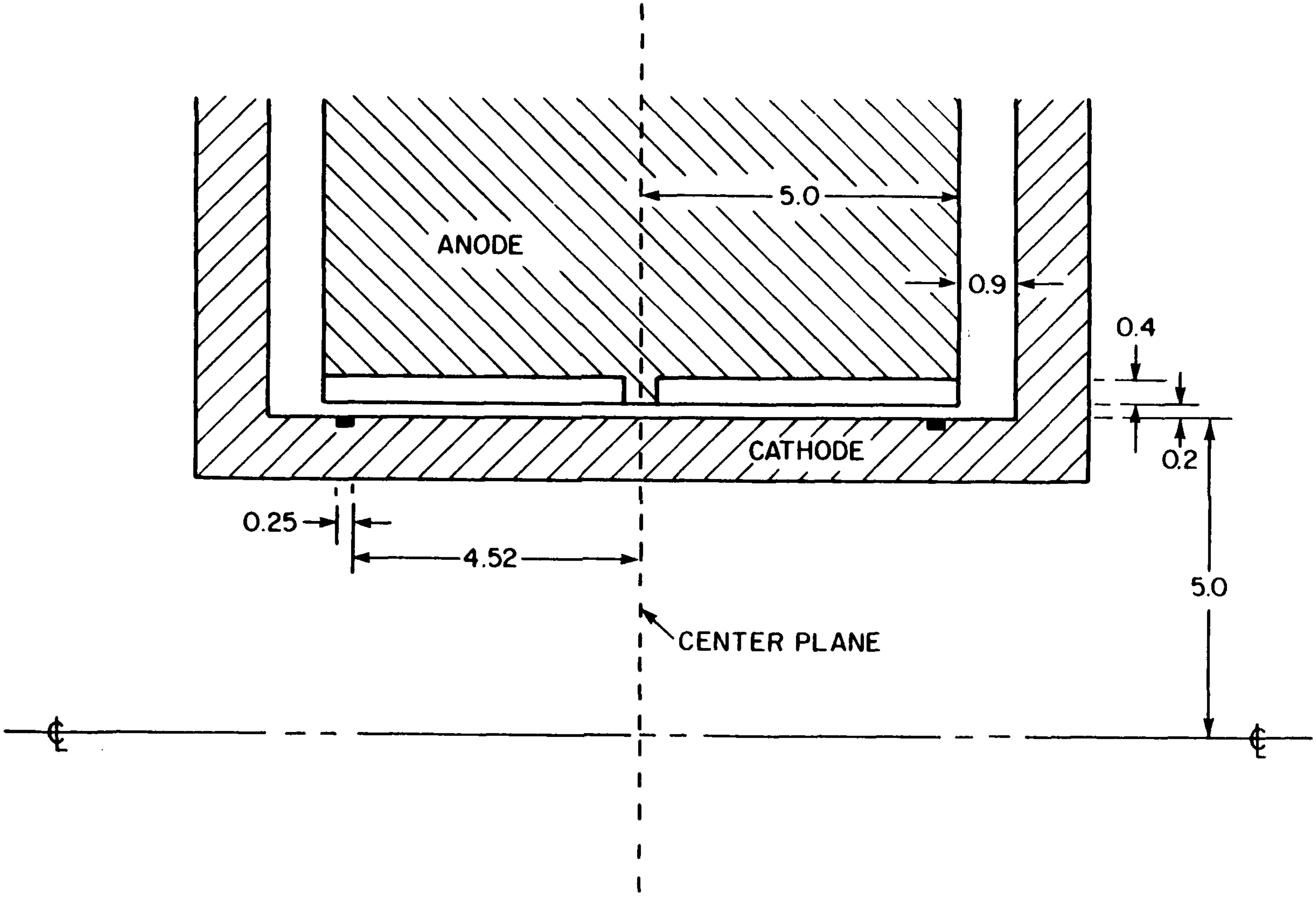

Fig. 3 — The radial enhanced ion diode (SHEPERD)

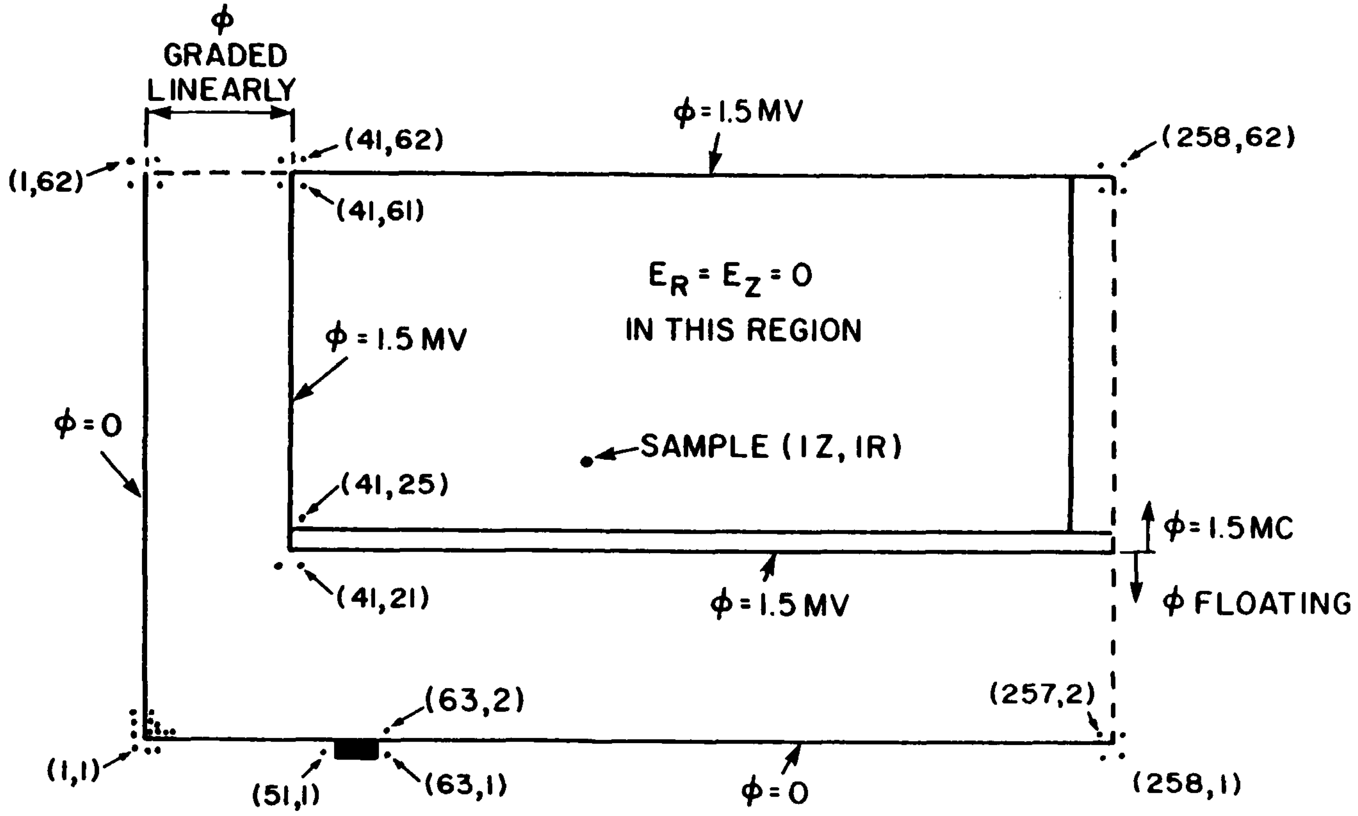

Fig. 4 — Computational region for SHEPERD simulations

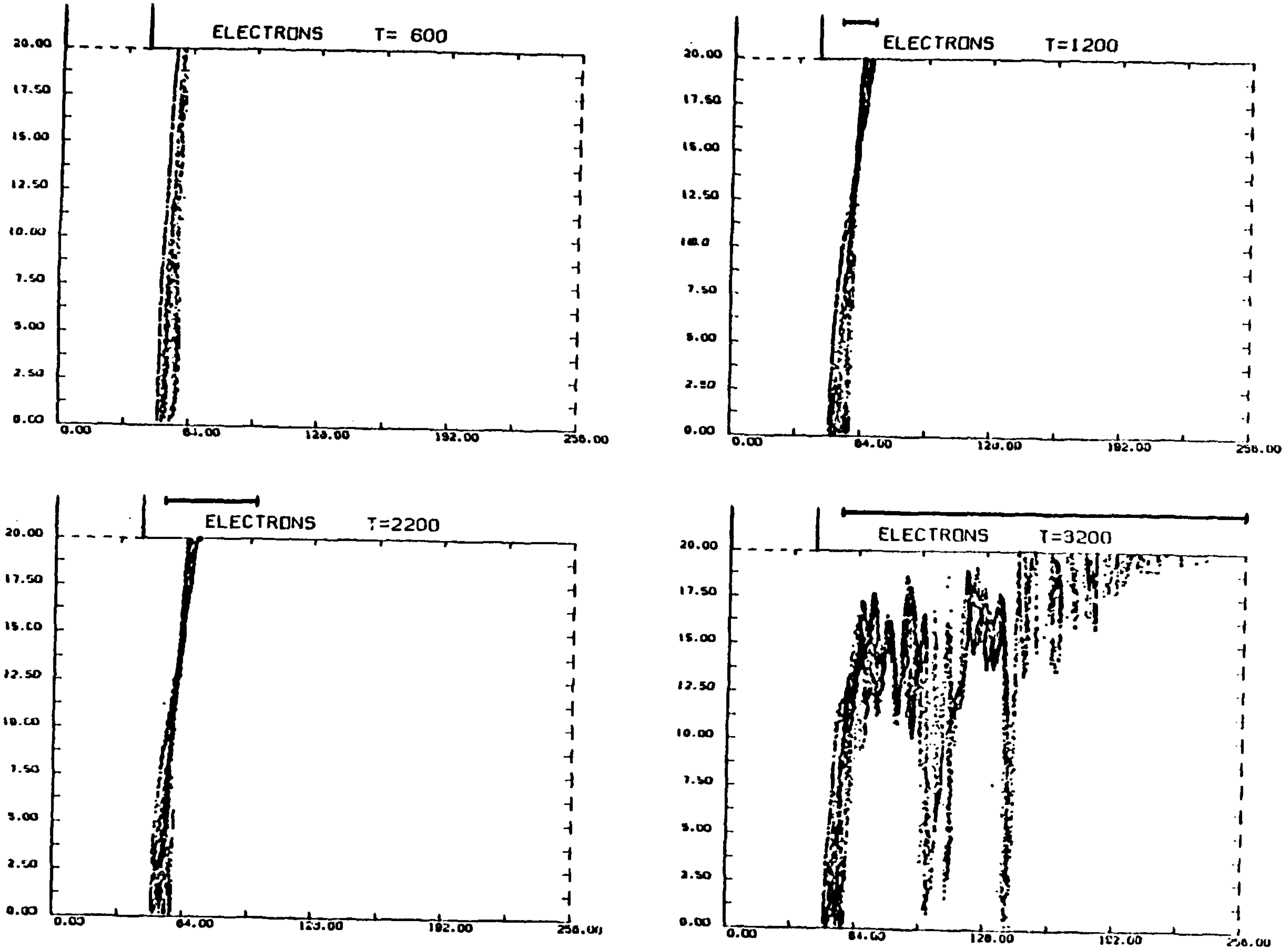

Fig. 5 — Equilibrium electron flows in SHEPERD with solid anode

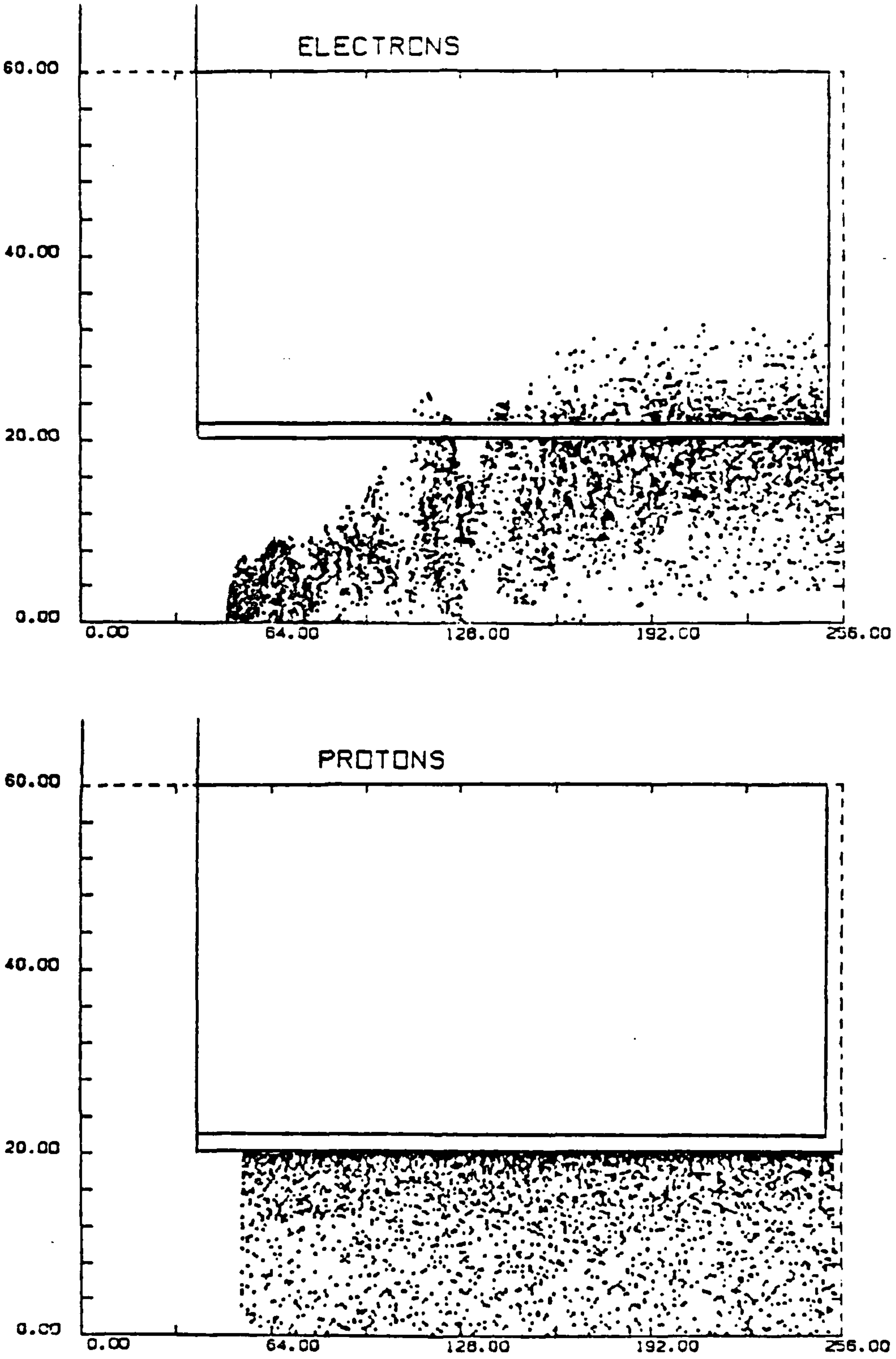

Fig. 6 — Equilibrium particle flows in SHEPERD with foil anode

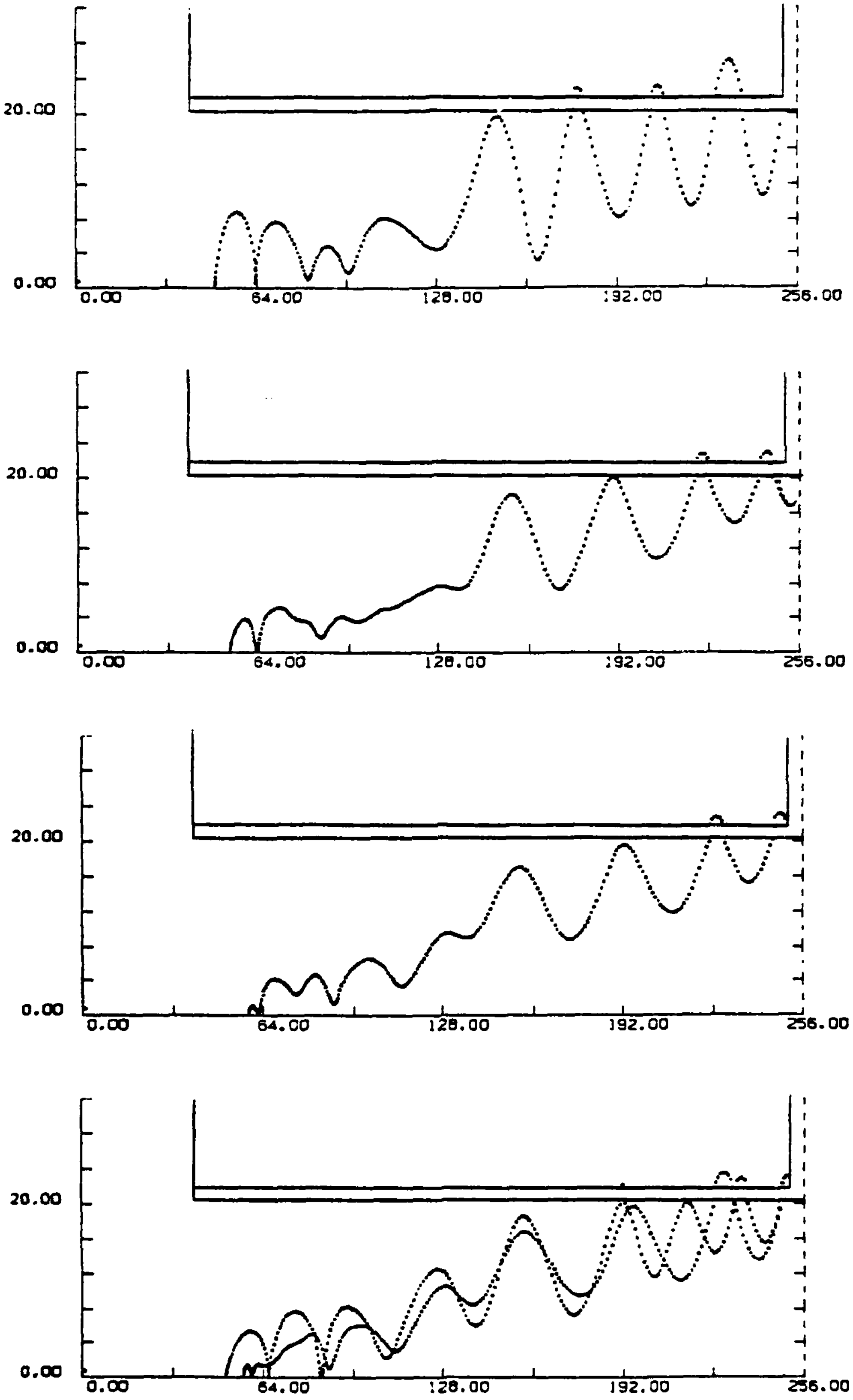

Fig. 7 — Sample electron trajectories in foil SHEPERD

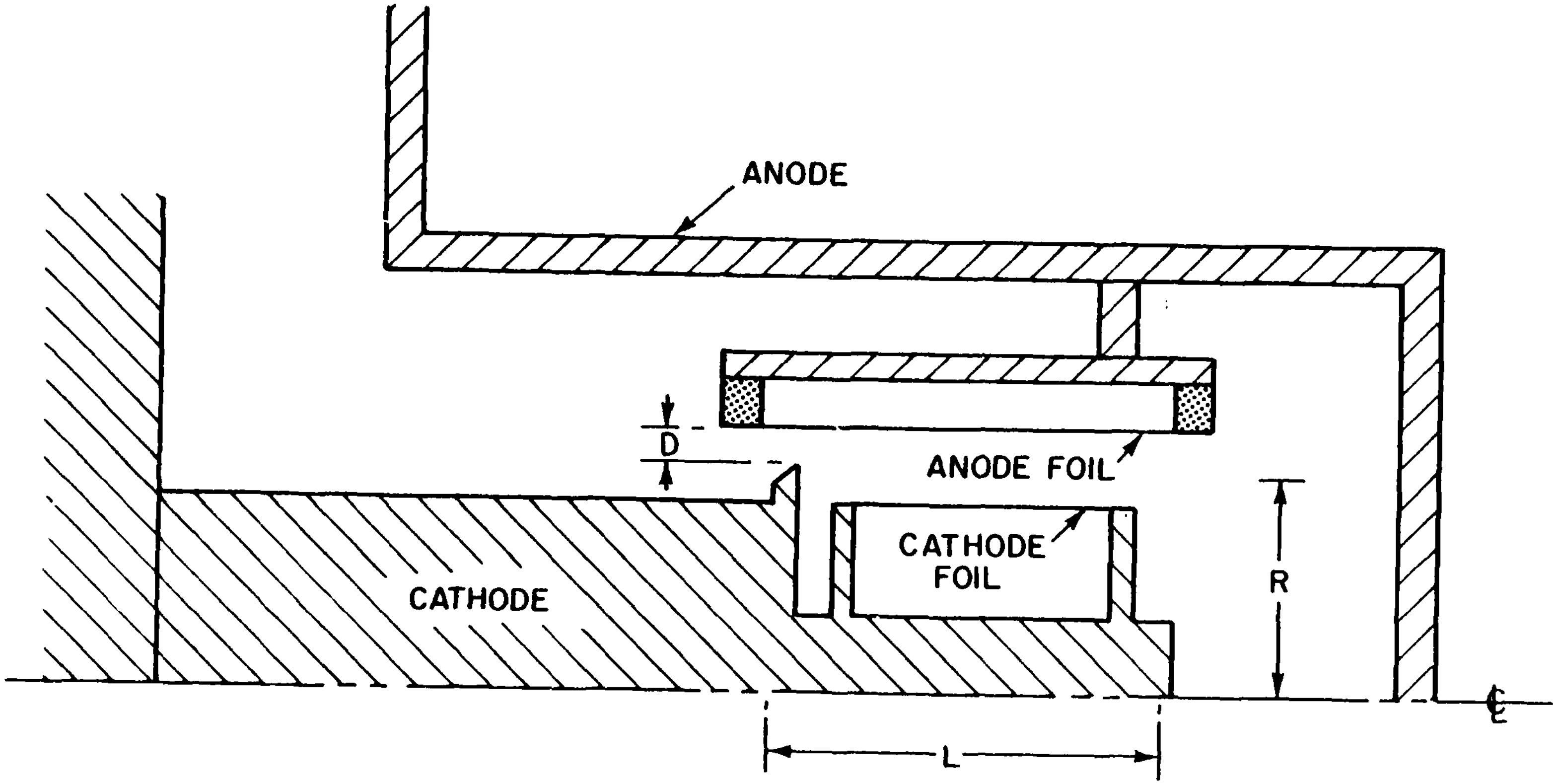

Fig. 8 — Experimental Gamble II half-SHEPERD schematic

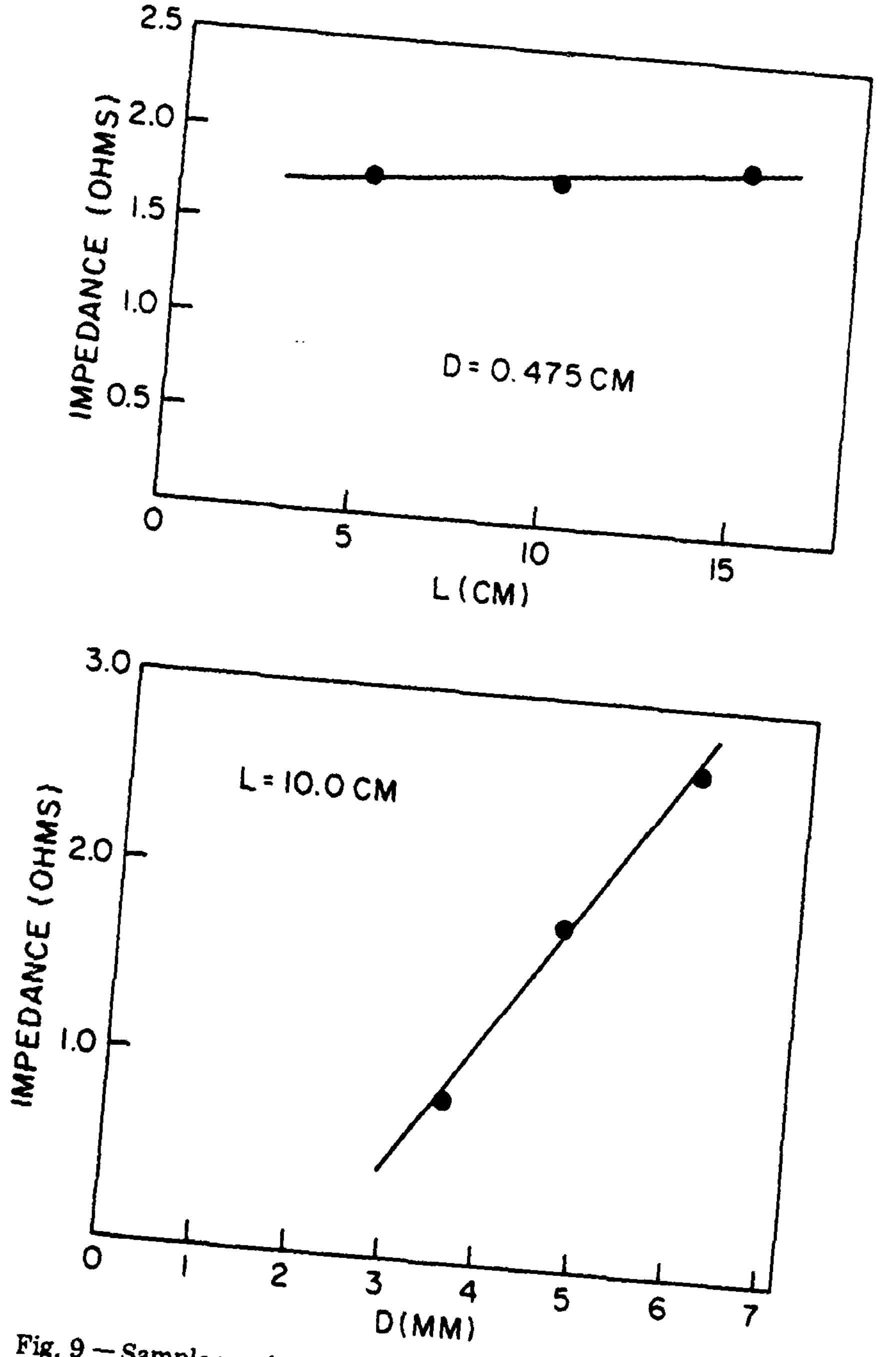

Fig. 9 — Sample results from experimental half-SHEPERD

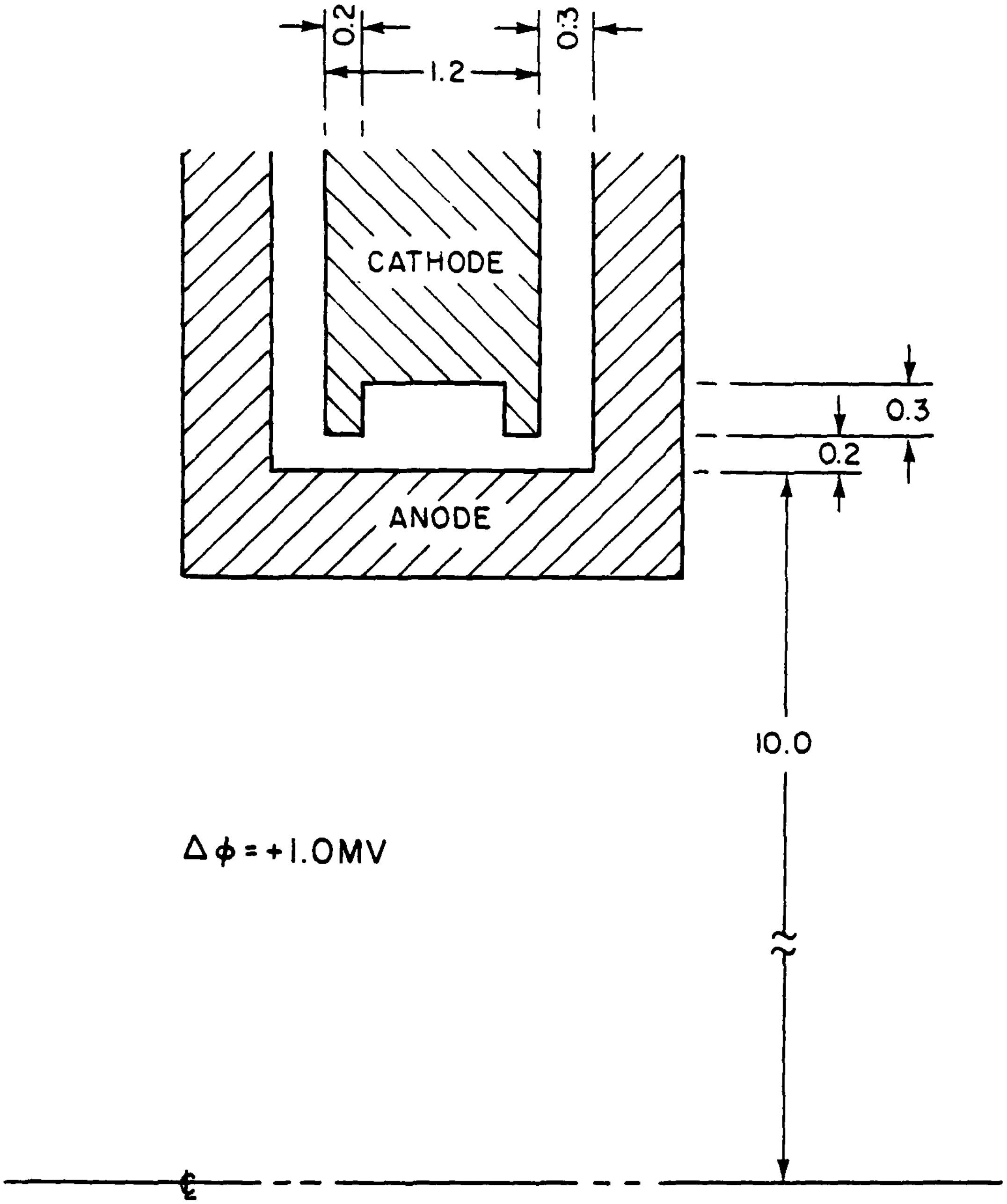

Fig. 10 — The radial enhanced electron diode

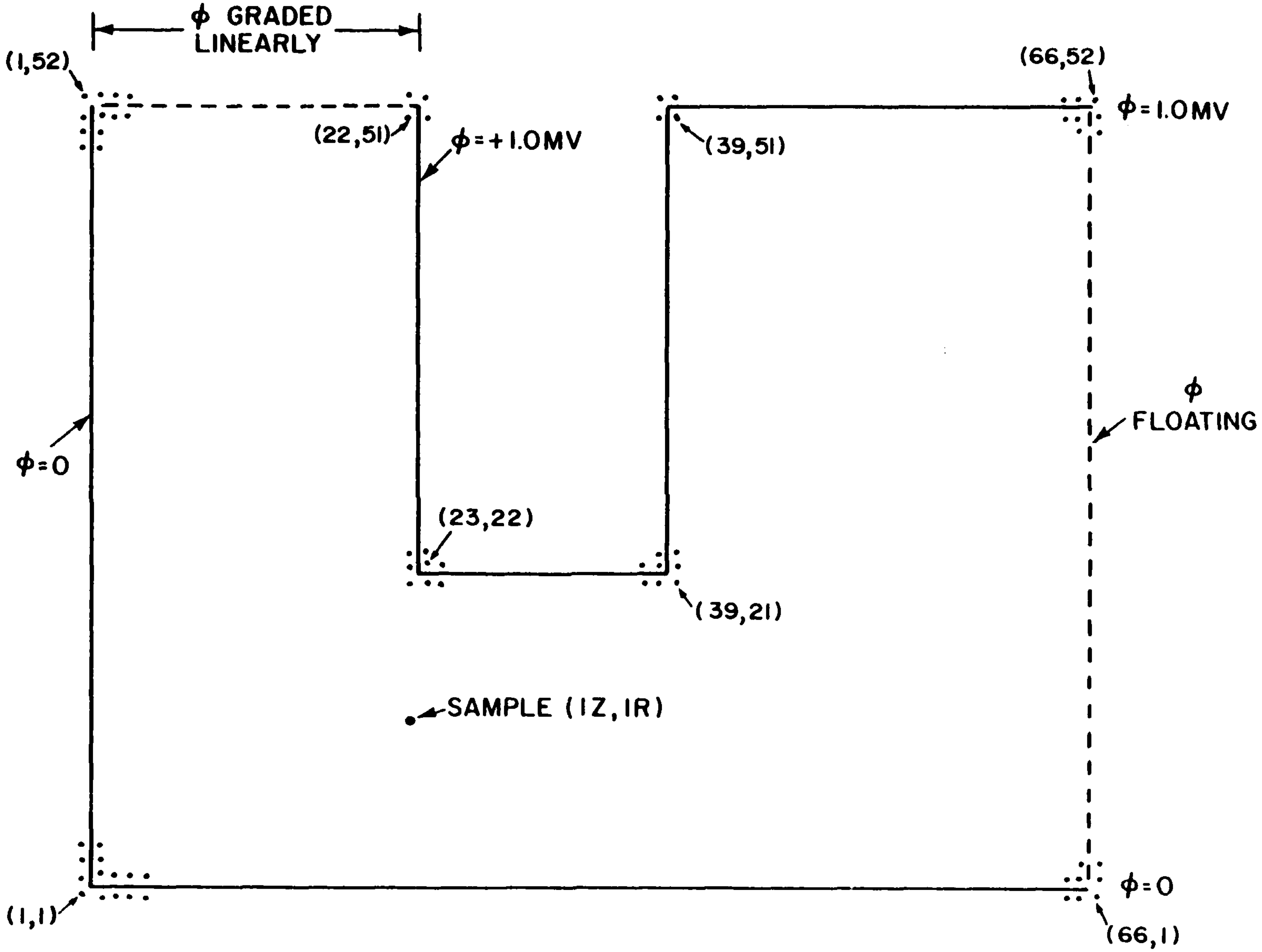

Fig. 11 — Computational region for radial enhanced electron diode

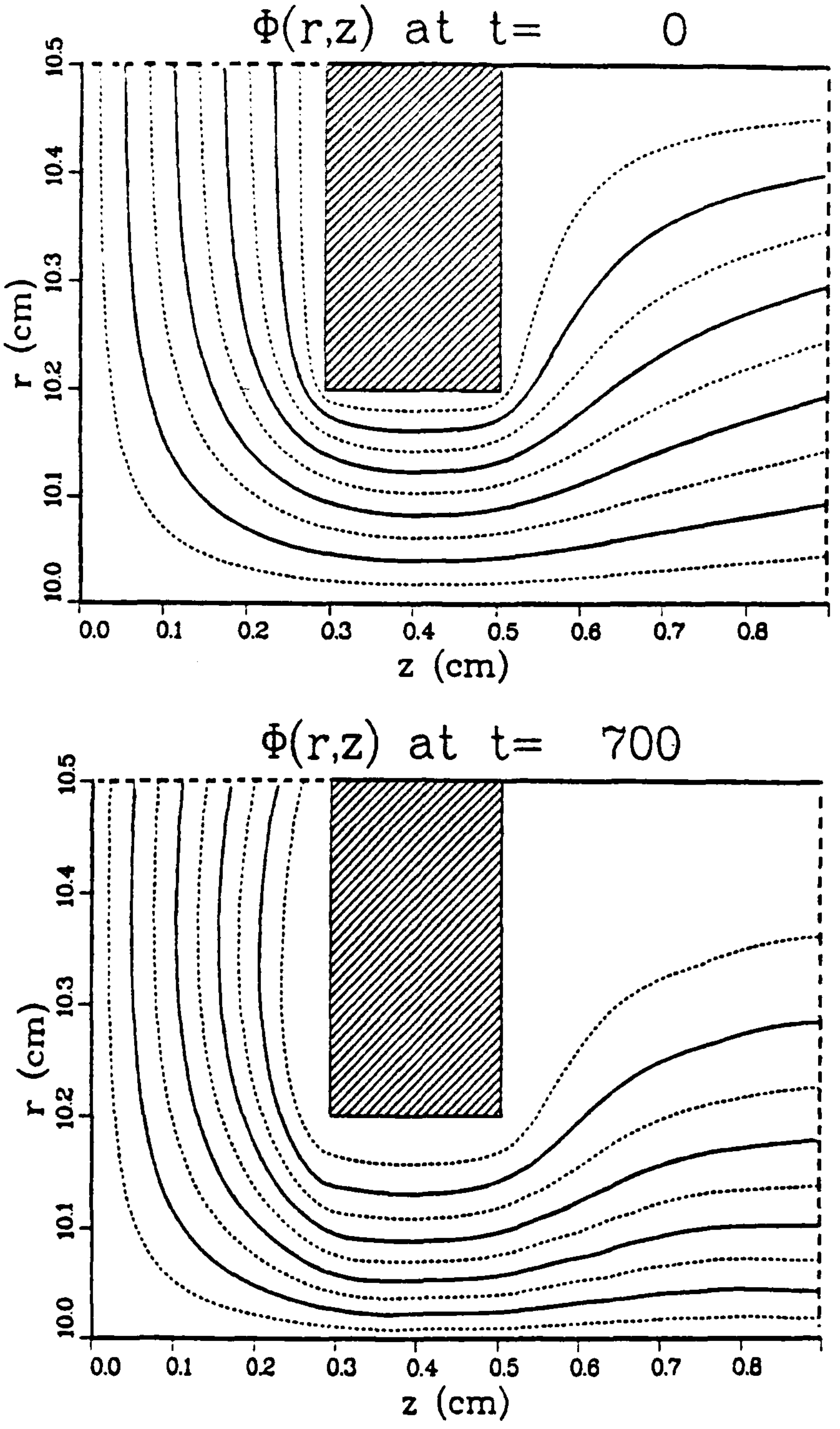

Fig. 12 — Equipotential plots for radial enhanced electron diode

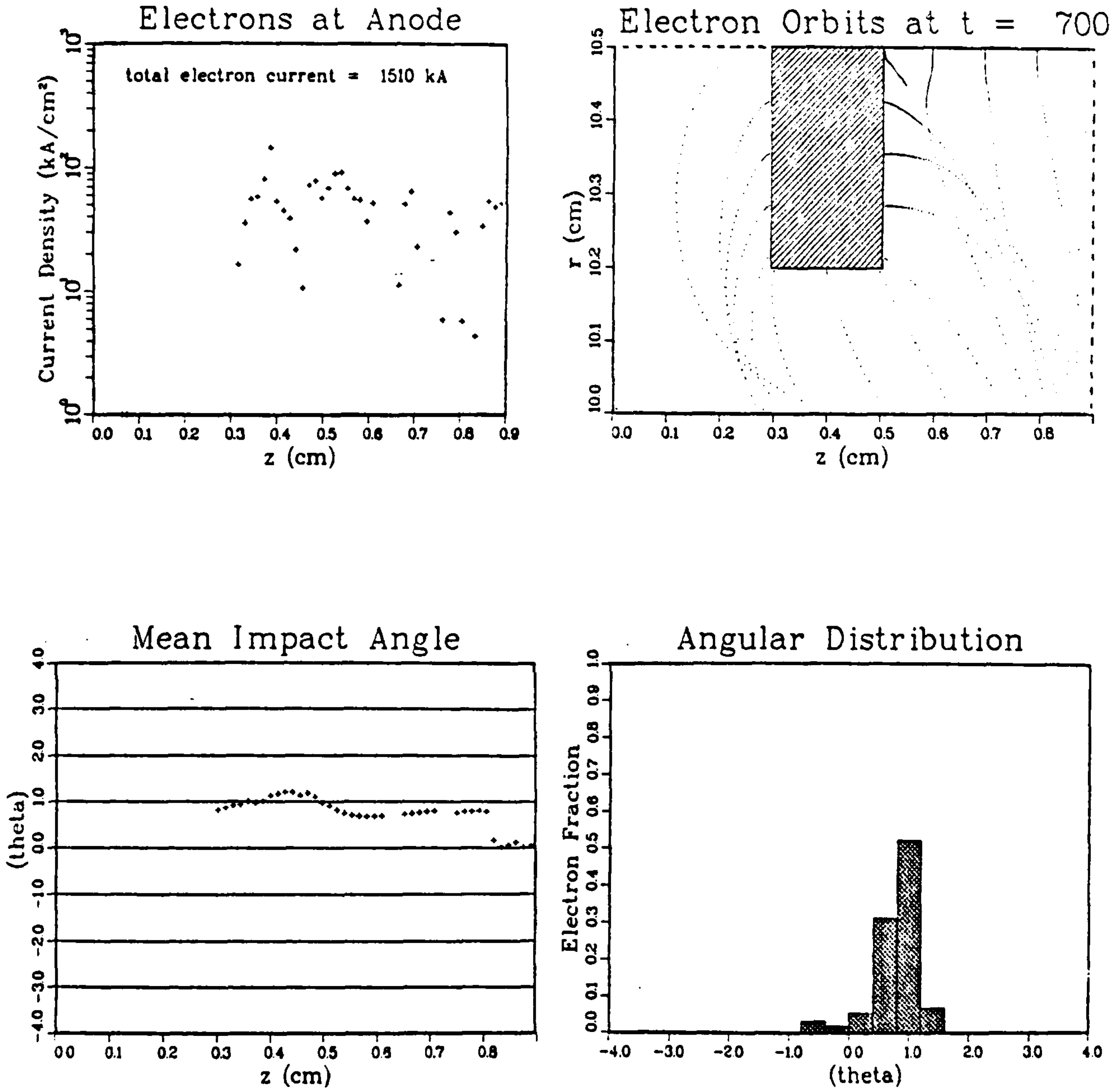

Fig. 13 — Results with only electrons in radial enhanced electron diode

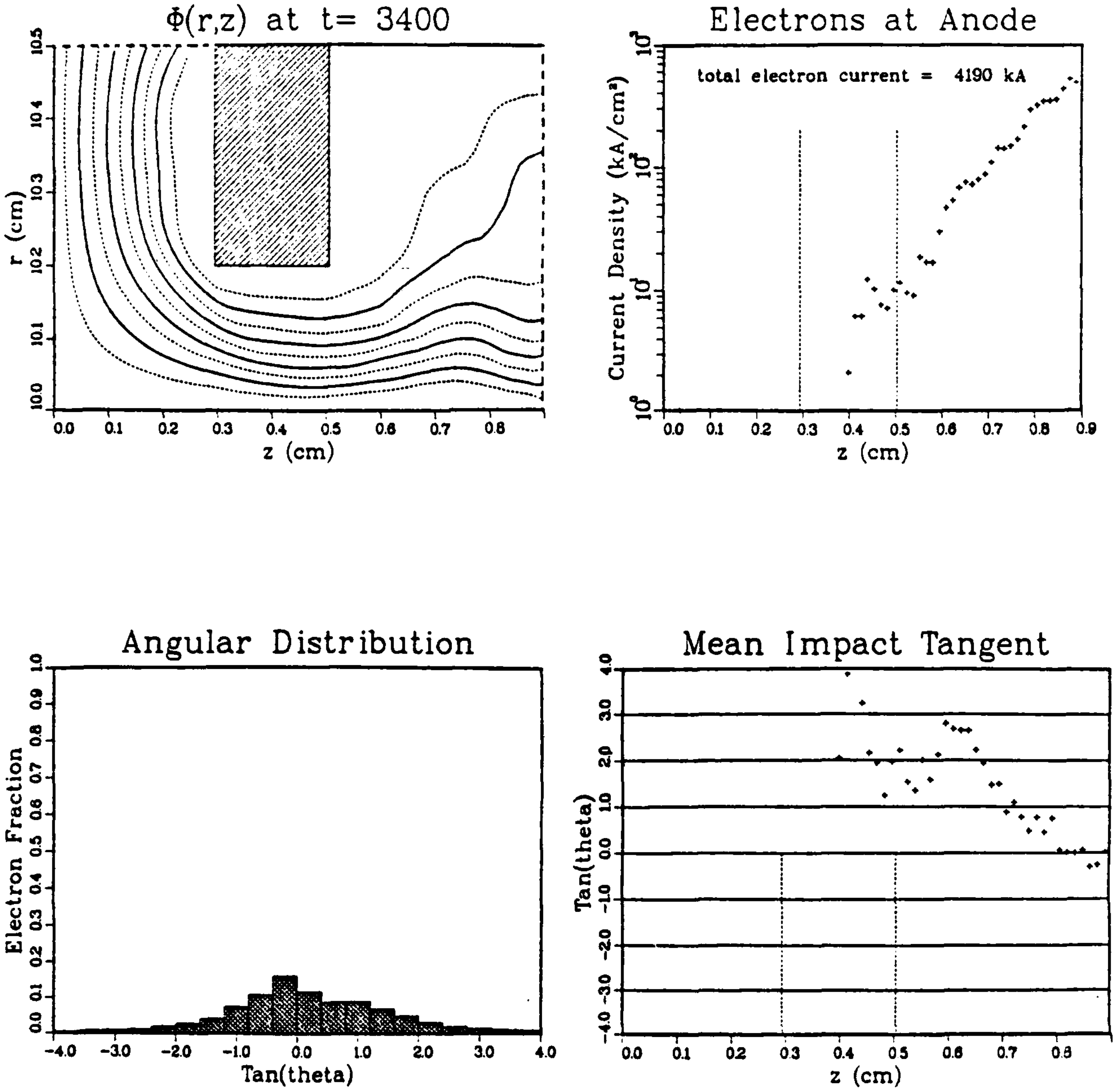

Fig. 14 — Results with ions and electrons in radial enhanced electron diode

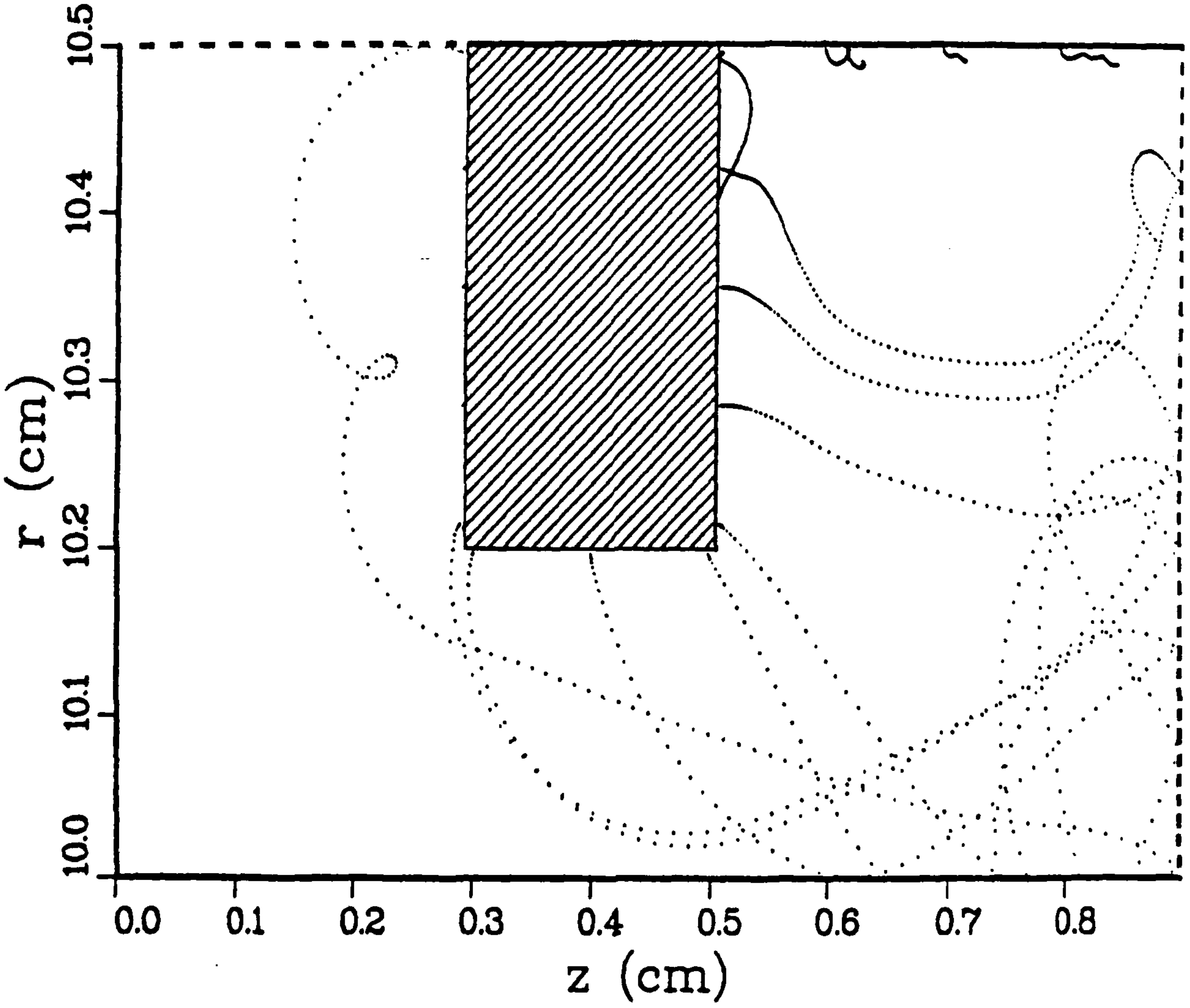

Fig. 15 — Sample electron trajectories in radial enhanced electron diode

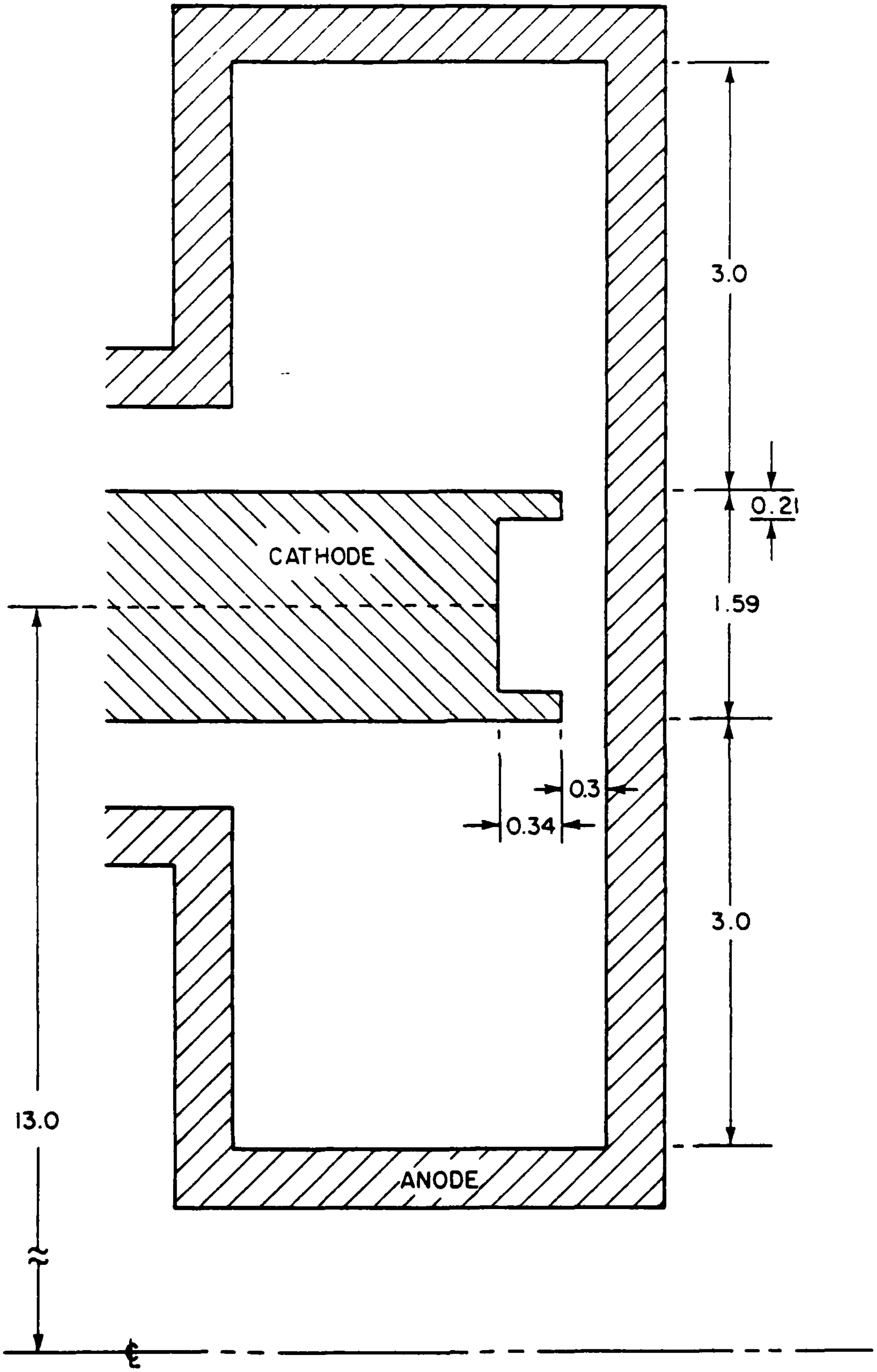

Fig. 16 — The magnetically insulated splitter (MIS) diode

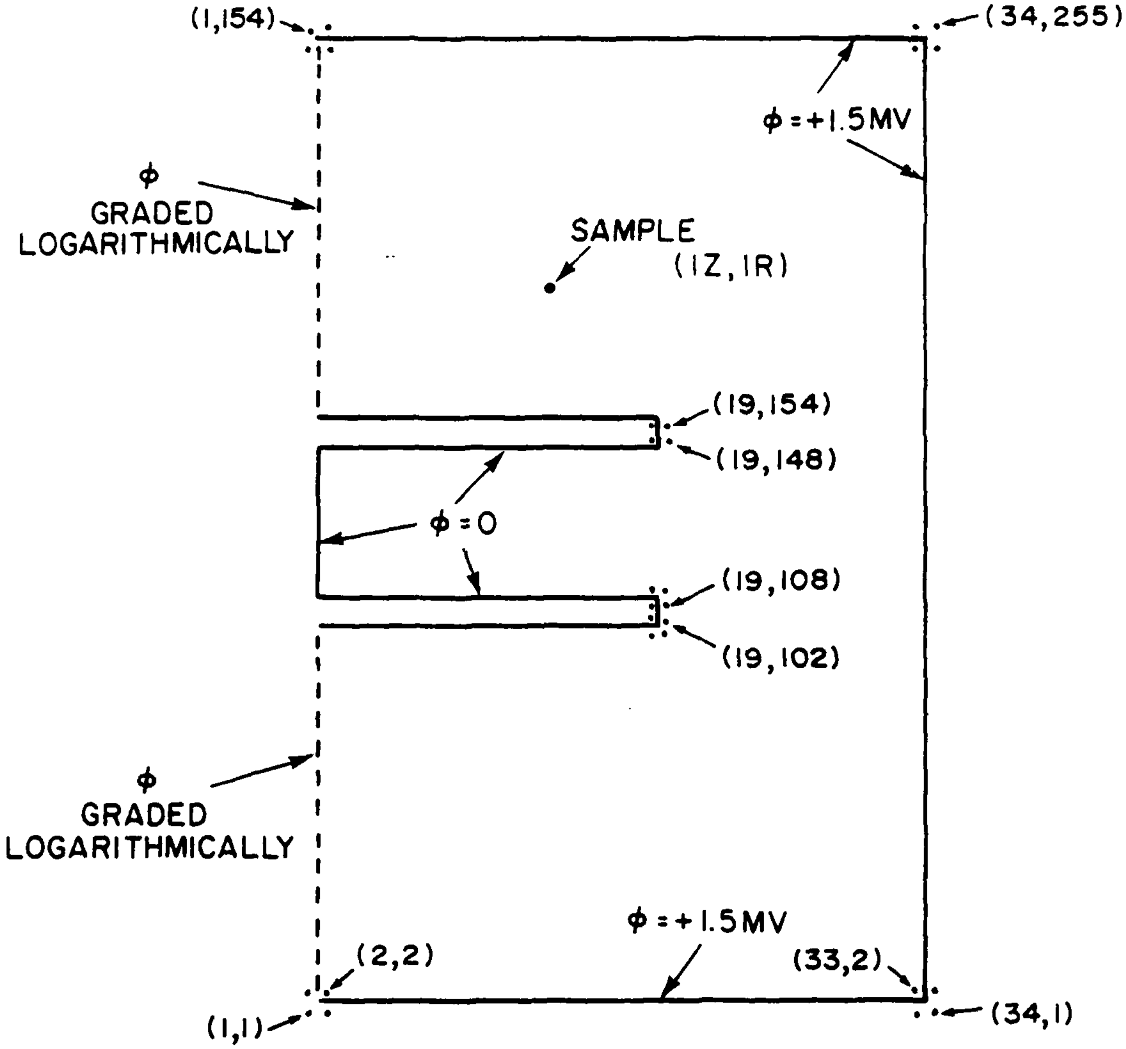

Fig. 17 — Computational region for MIS simulation

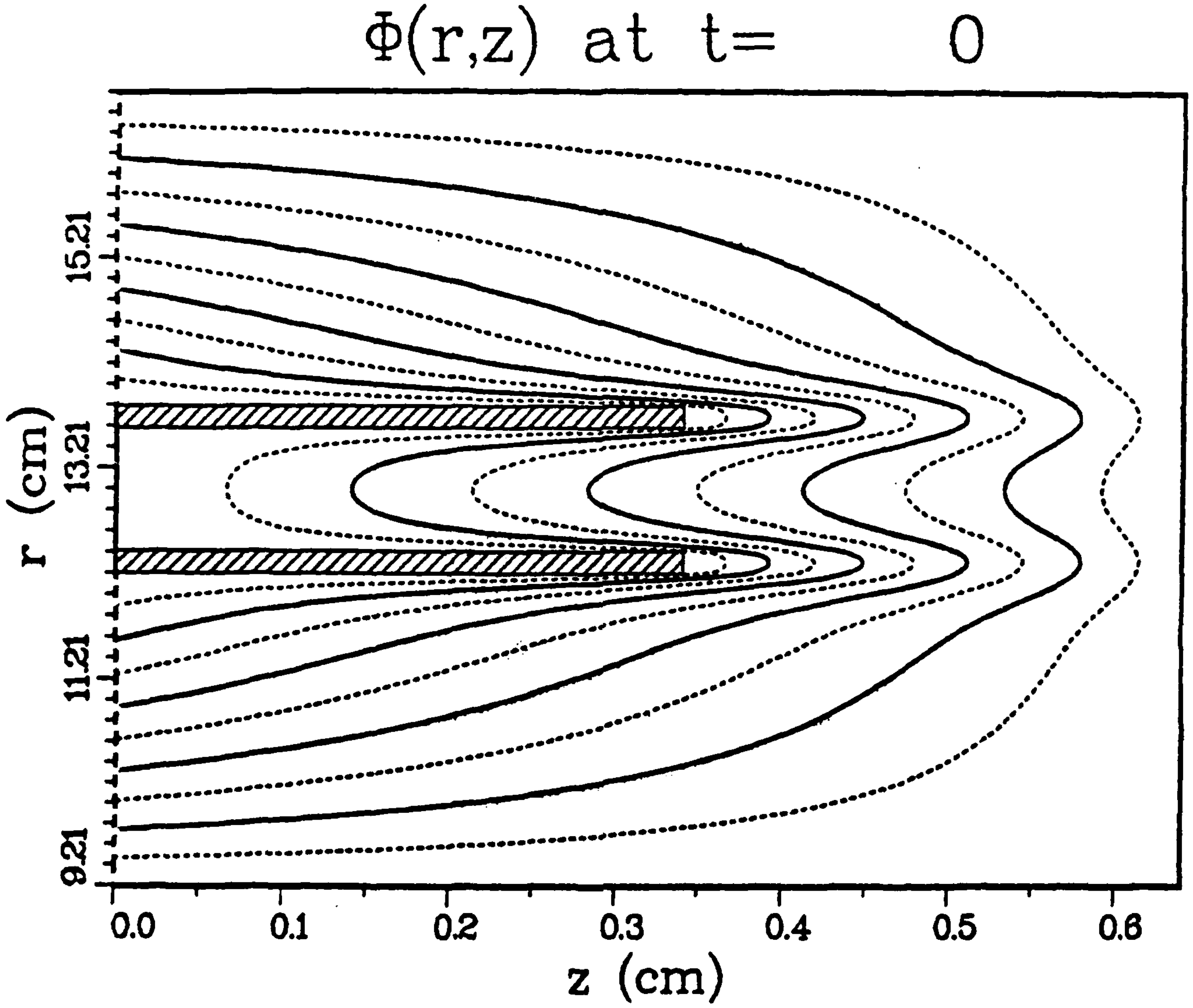

Fig. 18 — Source-free equipotential plot for MIS diode

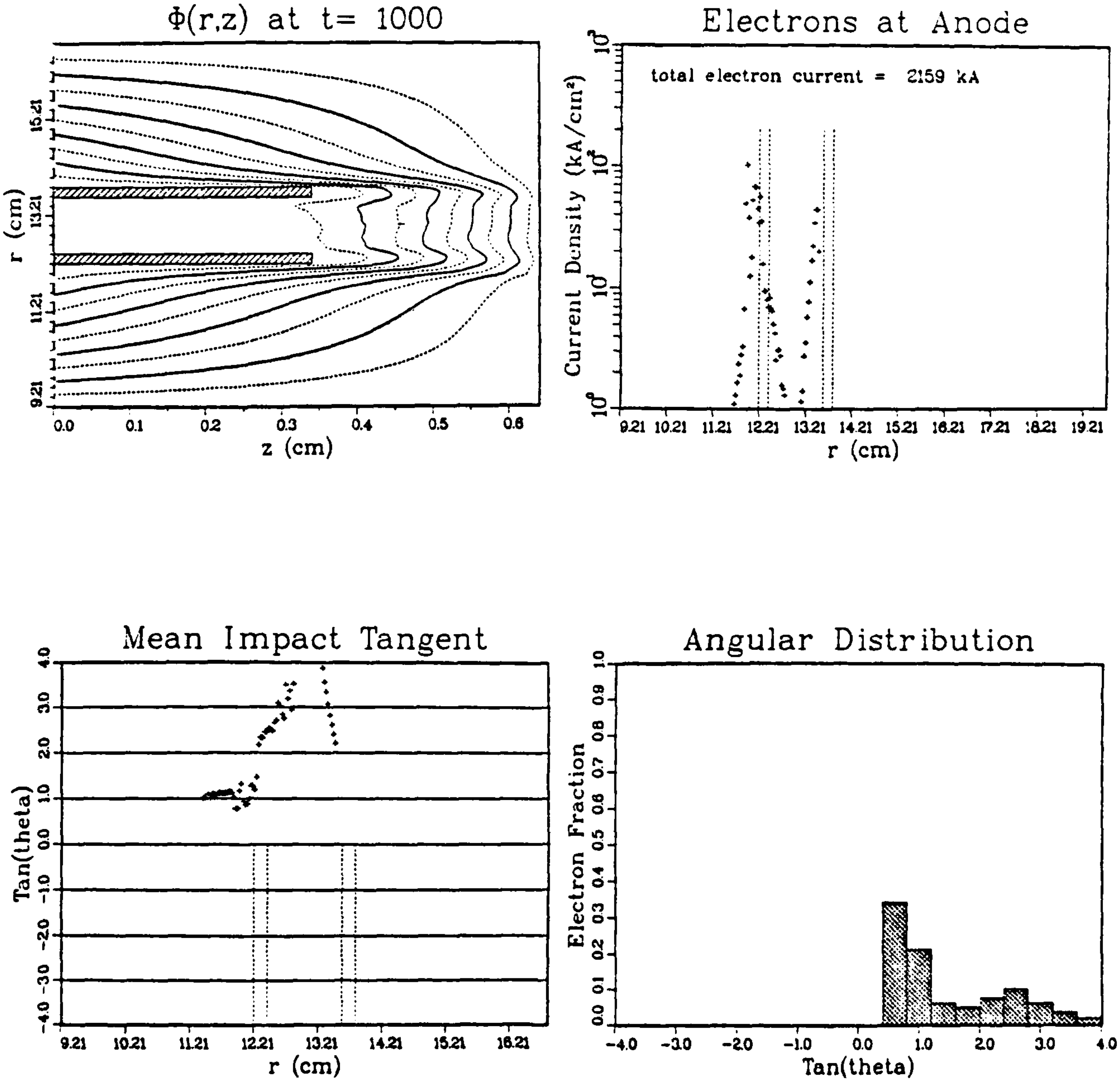

Fig. 19 — Results for single cathode electrons-only MIS diode
with 50% MIS current

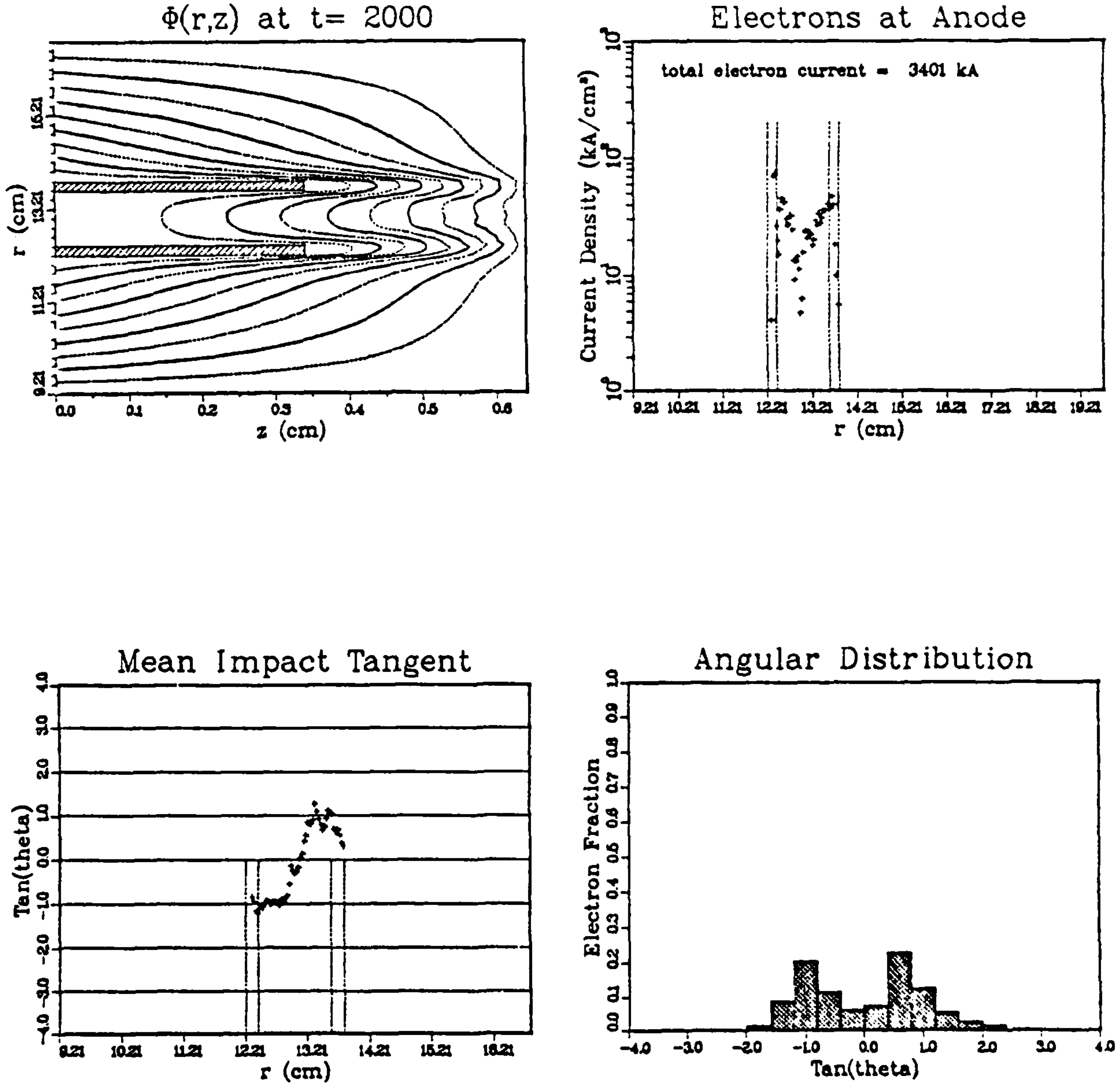

Fig. 20 — Results for electrons-only MIS diode with 50% MIS current

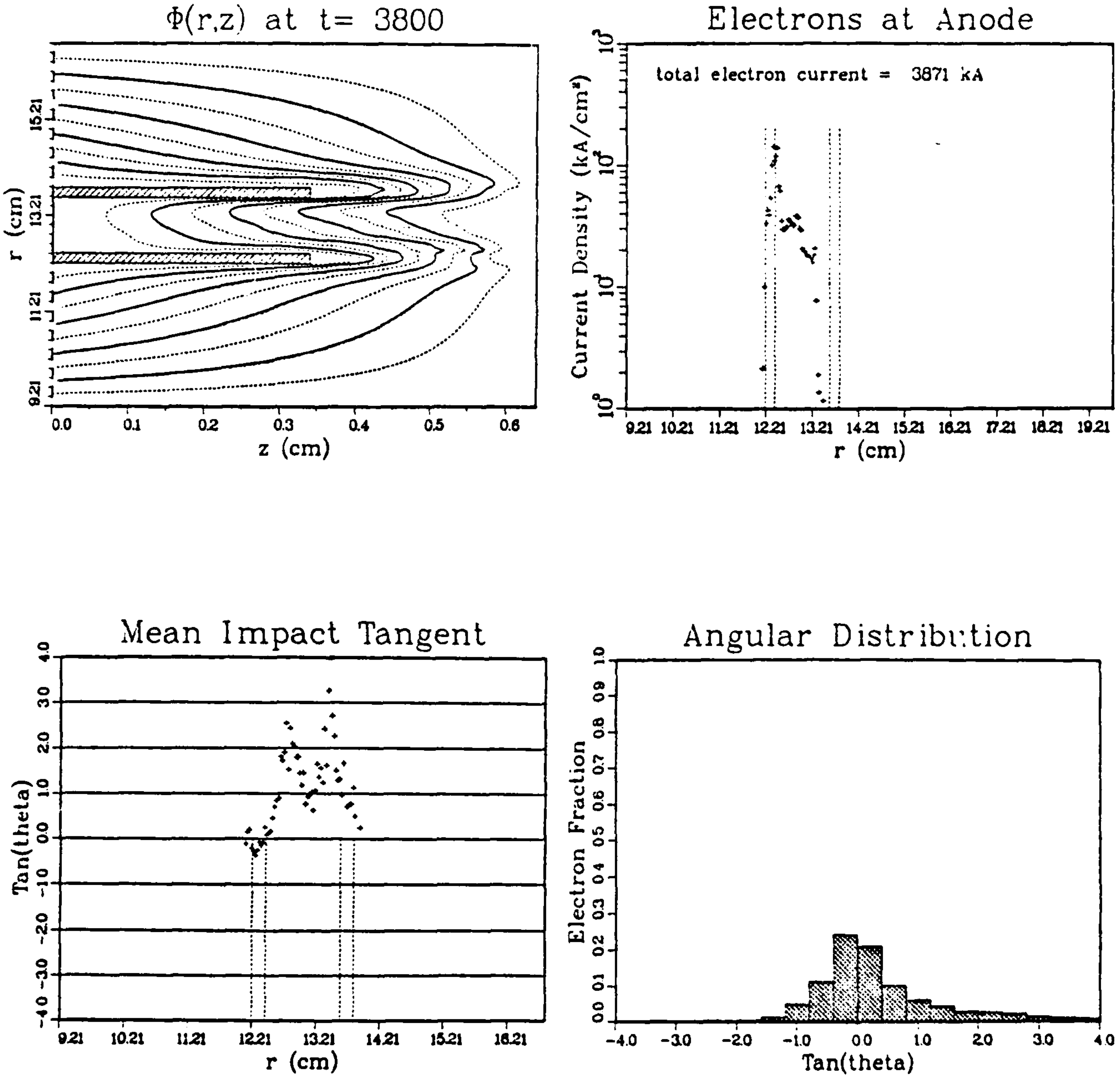

Fig. 21 — Results for ions-and-electrons MIS diode with 50% MIS current

REFERENCES

1. S.A. Goldstein and R.E. Lee, Phys. Rev. Lett. 35, 1079 (1975).

2. S.A. Goldstein, R.C. Davidson, J.G. Siambis and R.E. Lee, Phys. Rev. Lett. 33, 1471 (1974).

3. G. Cooperstein and J.J. Condon, J.Appl. Phys. 46, 1535 (1975).

4. S.J. Stephanakis, D. Mosher, G. Cooperstein, J.R. Boller, J. Golden, and S.A. Goldstein, Phys. Rev. Lett. 37, 1543 (1976).

5. D.J. Johnson, S.A. Goldstein, R.E. Lee, and W.F. Oliphant, J. Appl Phys. 49, 4634 (1978).

6. S.A. Goldstein, G. Cooperstein, R.E. Lee, D. Mosher, and S.J. Stephanakis, Phys. Rev. Lett. 40, 1504 (1978).

7. R.J. Barker, S.A. Goldstein, and R.E. Lee, Naval Research Laboratory (NRL) Memorandum Report 4279 (1980).

8. J.M. Credon, J. of Appl. Phys. 46, 2946 (1975).

9. S.J. Stephanakis, S.A. Goldstein, R.J. Barker, J.R. Boller, and G. Cooperstein, Bull. Am. Phys. 27, 992 (1982).

10. Experiments conducted at Sandia National Laboratories under the name, OBI, first by Dr. John Olsen and then by Dr. Steve Rosenthal (1981-2).

11. R.J. Barker and S.A. Goldstein, NRL Memorandum Report 4773 (1982).

12. R.J. Barker, S.A. Goldstein, and A.T. Drobot, NRL Memorandum Report 4642 (1981).

13. S.J. Stephanakis, J.R. Boller, G. Cooperstein, S.A. Goldstein, D.D. Hinshelwood, D. Mosher, W.F. Oliphant, F.L. Sandel, and F. C. Young, Bull. Am. Phys. Soc. 23, 907 (1978).

14. R.J. Barker, A.T. Drobot, R. Lee, and S.A. Goldstein, Proc. of the 9th Conf on the Numberical Simulation of Plasma, Evanston, IL (1980).

15. R.J. Barker and S.A. Goldstein, NRL Memorandum Report 4915 (1982).

16. R.J. Barker and S.A. Goldstein, Bull. Am. Phys. Soc. 26, 921 (1981).

17. J.W. Shearer, Lawrence Livermore Laboratory Report UCRL-52129 (1976).

18. F.L. Sandel, private communication.

19. R.J. Barker and S.A. Goldstein, NRL Memorandum Report 4837 (1982)

20. R.J. Barker, S.A. Goldstein, S.J. Stephanakis, and G. Cooperstein, Bull. Am. Phys. Soc. 27, 991 (1982).

21. J. Pearlman and J. Shannon, private communication.

22. R.J. Barker and P.F. Ottinger, NRL Memorandum Report 4654 (1981).

23. R.A. Meger, R.J. Barker, et al., IEEE Int. Conf. on Plasma Science, Santa Fe, New Mexico (1981).

24. A.T. Drobot, R.J. Barker, and S.A. Goldstein, IEEE Int. Conf. on Plasma Science, Madison, Wisconsin (1980).

DNA DISTRIBUTION LIST

Director
Defense Nuclear Agency
Washington, DC 20305
Attn: TISI Archieves 1 copy
TITL Tech. Library 3 copy
J. Z. Farber (RAEV) 1 copy
H. Soo 1 copy
M. Fellows 1 copy

Air Force Office of Scientific Research
Physics Directorate
Bolling AFB, DC 20332
Attn: A. K. Hyder 1 copy
M. A. Stroscio 1 copy

Air Force Weapons Laboratory, AFSC
Kirtland, AFB, NM 87117
Attn: NTYP (W. L. Baker) 1 copy

Atomic Weapons Research Establishment
Building H36
Aldermaston, Reading RG 7 4PR
United Kingdom
Attn: J. C. Martin 1 copy

Boeing Company, The
P.O. Box 3707
Seattle, WA 98124
Attn: Aerospace Library 1 copy

Brookhaven National Laboratory
Upton, NY 11973
Attn: A. F. Maschke 1 copy

BMO/EN
Norton AFB, CA
Attn: ENSN 1 copy

Cornell University
Ithaca, NY 14850
Attn: D. A. Hammer 1 copy
R. N. Sudan 1 copy

Commander
Harry Diamond Laboratory
2800 Powder Mill Rd.
Adelphi, MD 20783
(CNWDI-INNER ENVELOPE: ATTN: DELHD-RBH)
Attn: DELHD-NP 1 copy
DELHD-RCC-J.A. Rosando 1 copy
DRXDO-RBH-K. Kerris 1 copy
DRXDO-TI-Tech Lib. 1 copy

Defense Advanced Research Project Agency
1400 Wilson Blvd.
Arlington, VA 22209
Attn: R. L. Gullickson 1 copy

Defense Technical Information Center
Cameron Station
5010 Duke Street
Alexandria, VA 22314
Attn: T.C. 2 copy

JAYCOR, Inc.
205 S. Whiting Street
Alexandria, VA 22304
Attn: J. Guillory 1 copy

Kaman Tempo
816 State Street (P.O. Drawer QQ)
Santa Barbara, CA 93102
Attn: DASIAC

Lawrence Berkeley Laboratory
Berkeley, CA 94720
Attn: D. Keefe 1 copy

Lawrence Livermore National Laboratory
P.O. Box 808
Livermore, CA 94550
Attn: Tech. Info. Dept. L-3 1 copy
D. J. Meeker

Los Alamos National Laboratory
P.O. Box 1663
Los Alamos, NM 87545
Attn: M. Gillispie/Theo. Div. 1 copy

Massachusetts Institute of Technology
Cambridge, MA 02139
Attn: R. C. Davidson 1 copy
G. Bekefi 1 copy

Maxwell Laboratories, Inc.
9244 Balboa Avenue
San Diego, CA 92123
Attn: J. Pearlman 1 copy

Mission Research Corporation
1400 San Mateo Blvd. SE
Albuquerque, NM 87108
Attn: B. B. Godfrey 1 copy

National Science Foundation
Mail Stop 19
Washington, DC 20550
Attn: D. Berley 1 copy

Naval Research Laboratory
Addressee: Attn: Name/Code
Code 2628 - TID Distribution 22 copies
Code 1001 - T. Coffey 1 copy
Code 4040 - J. Boris 1 copy
Code 4700 - S. L. Ossakow 26 copies
Code 4704 - C. Kapetanakos 1 copy
Code 4720 - J. Davis 1 copy
Code 4730 - S. Bodner 1 copy
Code 4740 - V. Granatstein 1 copy
Code 4760 - B. Robson 1 copy
Code 4770 - I. M. Vitkovitsky 10 copies
Code 4771 - D. Mosher 10 copies
Code 4771 - F. C. Young 1 copy
Code 4773 - G. Cooperstein 10 copies
Code 4773 - S. J. Stephanakis 1 copy
Code 4790 - D. Columbant 1 copy
Code 4790 - I. Haber 1 copy
Code 4790 - M. Lampe 1 copy
Code 6682 - D. Nagel 1 copy

Physics International Co.
2700 Merced Street
San Leandro, CA 94612
Attn: A. J. Toepfer 1 copy

Pulse Sciences, Inc.
1615 Broadway, Suite 610
Oakland, CA 94612
Attn: S. Putnam 1 copy

R&D Associates
Suite 500
1401 Wilson Blvd.
Arlington, VA 22209
Attn: P. J. Turchi 1 copy

R&D Associates
P.O. Box 9695
Marina Del Rey, CA 90291
Attn: C. MacDonald 1 copy

Sandia National Laboratories
P.O. Box 5800
Albuquerque, NM 87185
Attn: G. W. Kuswa/1240 1 copy
T. Martin/1250 1 copy
J. P. Vandevender/1260 1 copy
G. Yonas/1200 1 copy

Spire Corporation
P.O. Box D
Bedford, MA 01730
Attn: R. G. Little 1 copy

Stanford University
SLAC
P.O. Box 4349
Stanford, CA 94305
Attn: W. B. Herrmannsfeldt 1 copy

University of California
Irvine, CA 92717
Attn: N. Rostoker 1 copy

University of Washington
Dept. of Nuclear Engineering
BF-10
Seattle, WA 98115
Attn: F. Ribe 1 copy

U.S. Department of Energy
Division of Inertial Fusion
Washington, DC 20545
Attn: T. F. Godlove 1 copy
S. L. Kahalas 1 copy
R. L. Schriever 1 copy

U.S. Department of Energy
P.O. Box 62
Oak Ridge, TW 37830 1 copy